Supplementary Material

A molecule with half-Möbius topology

Authors: Igor Rončević[1,2#*], Fabian Paschke[3#], Yueze Gao[2], Leonard-Alexander Lieske[3], Lene A. Gödde[2], Stefano Barison[4,5], Samuele Piccinelli[4,6], Alberto Baiardi[4], Ivano Tavernelli[4], Jascha Repp[7], Florian Albrecht[3], Harry L. Anderson[2] and Leo Gross[3*]

Affiliations:

[1] Department of Chemistry, The University of Manchester, Oxford Road, Manchester, United Kingdom.

[2] Department of Chemistry, Oxford University, Chemistry Research Laboratory, Oxford, United Kingdom.

[3] IBM Research Europe – Zurich, Rüschlikon, Switzerland.

[4] IBM Quantum, IBM Research Europe – Zurich, Rüschlikon, Switzerland.

[5] Institute for Theoretical Physics, ETH Zürich, CH-8093 Zürich, Switzerland

[6] Institute of Physics, École Polytechnique Fédérale de Lausanne (EPFL), Lausanne, Switzerland

[7] Institute of Experimental and Applied Physics and Halle-Berlin-Regensburg Cluster of Excellence CCE, University of Regensburg, Regensburg, Germany.

[#] Equally contributing first authors

* Corresponding authors. Email: igor.roncevic@manchester.ac.uk; lgr@zurich.ibm.com

Table of Contents

1. STM and AFM methods

The on-surface characterization and reactions were performed in a home-built combined STM/AFM, operated at a temperature $T = 5$ K in ultra-high vacuum. The decachlorofluorene precursor **1** (*22*) was thermally sublimed onto a cold ($T < 10$ K) Au(111) surface partially covered with NaCl bilayer (two atomic layer thick) islands. AFM measurements were performed in non-contact mode with a qPlus sensor (*60*). The sensor was operated in frequency-modulation mode (*61*) with the oscillation amplitude A kept constant at $A = 0.5$ Å. All data were recorded on molecules adsorbed on bilayer NaCl with CO functionalized tips (*40*). STM images were recorded at constant current and AFM images at constant height. The STM-controlled setpoint for constant-height AFM images provides the tip height at the top center of the image at which position the tip-height offset Δz was added. For spectroscopy, the STM setpoint corresponds to the lateral tip position at which the spectra had been obtained. Positive tip-height offsets Δz correspond to an increase in tip-sample distance with respect to the setpoint. With AFM-far, we denote an imaging height just at the onset of atomic resolution. With AFM-close, we denote imaging at Δz further reduced by about few 0.1 Å, with respect to AFM-far. AFM images were acquired at $V = 0$ V, if not stated otherwise (in **fig. S15A**).

The bias voltage V was applied to the sample with respect to the tip. Dehalogenation of **1** and skeletal rearrangement towards a carbon ring was induced by applying voltage pulses with typically $V = 4.5$ V for a few 100 ms and at constant height with the tip above the molecule and the tip being retracted by 6 to 8 Å from a setpoint of $I = 1$ pA and $V = 0.2$ V, resulting in currents I on the order of few pA at $V = 4.5$ V (*22*).

2. Supplementary Schemes

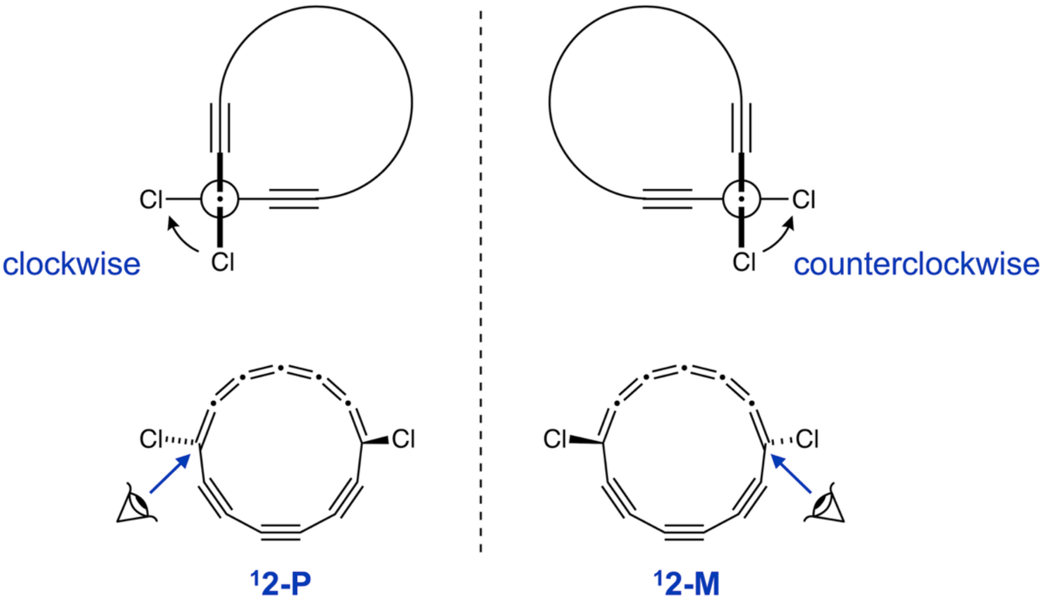

Scheme S1. **Nomenclature of ^{1}2-P and ^{1}2-M**. The out-of-plane locations of the Cl heteroatoms give rise to a helical twist. The Cl-C bonds are tilted out of the molecular plane by θ_1 and θ_2 (see **fig. S4**). In the **P** enantiomer, the rotation of the second C-Cl bond with respect to the first, upon moving through the shorter segment of the ring, in **2** the six-bond segment, is clockwise by $\varphi = \theta_1 + \theta_2$, whereas in the **M** enantiomer it is counterclockwise by φ. Positive (negative) angles correspond to clockwise (counterclockwise) rotations. The sign of the tilt angles θ_1 and θ_2 is defined with respect to movement form the shorter segment to the longer segment. With these definitions, positive (negative) tilt angle φ and twist angles θ_1, θ_2 are observed in ^{1}**2-P** (^{1}**2-M**). The diagrams in the top row show a view parallel to the shorter segment and the resulting twist angles φ. Note that the winding of the half-Möbius orbital basis is left-handed (anticlockwise) in ^{1}**2-P** and in hypothetical ^{1}**4-P**, see **Scheme S2**, because in these the shorter segment has an even number of bonds, but right-handed (clockwise) in hypothetical ^{1}**3-P**, because in it the shorter segment has an odd number of bonds.

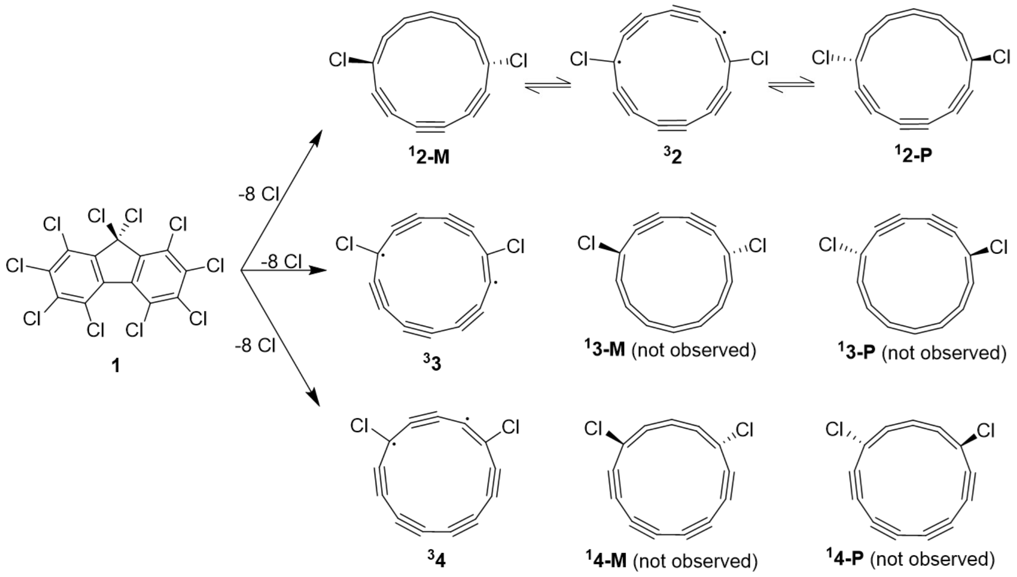

Scheme S2. Expanded reaction scheme, showing other isomers of $C_{13}Cl_2$. From **1** we generated **2**, **3** and **4** by tip-induced dissociation of 8 Cl atoms. As discussed in the main text, **2** was observed in the singlets ^{1}**2-M** and ^{1}**2-P** and the triplet ^{3}**2**. For **3**, we only observed the planar triplet ^{3}**3** (see **fig. S11**). For **4**, we only observed the planar triplet ^{3}**4** (see **fig. S12**).

3. Computational details

3.1. Tight-binding calculations

Following the approach of Garner and Hoffman (*2*), a tight-binding nearest-neighbor Hamiltonian for linear carbon chains with *N* sp-hybridized atoms can be written as:

$$\widehat{H}_{nn} = -\sum_{\langle i,j\rangle}^{N} \sum_{\langle k,l\rangle}^{2} t_{kl} c_{ik}^{\dagger} c_{jl} \tag{1}$$

in which $\langle i, j\rangle$ denotes summation over neighboring atoms *i* and *j*, and $\langle k, l\rangle$ denotes summation over two orthogonal *p*-orbitals (green and purple in **fig. S1**), which are coupled by t_{kl}. In the case that *i* or *j* is sp^2-hybridized, the sum only runs to 1. The t_{kl} coupling depends on the angle between the orbitals *k* and *l* on neighboring atoms *i* and *j*:

$$t_{kl} = t_0 \cos\phi_{ijkl} \tag{2}$$

In a non-helical topology, we can assign these orbitals as p_z, (e.g., when $k, l = 1$), and p_{xy} $(k, l = 2)$, which gives trivial solutions:

$$k = l\colon \phi_{ij11} = \phi_{ij22} = 0;\ t_{kl} = t_0 \tag{3}$$

$$k \neq l\colon \phi_{ij12} = \phi_{ij21} = \frac{\pi}{2};\ t_{kl} = 0 \tag{4}$$

In a helical basis shown in **fig. S1** an angle of 2θ is accumulated over *N* atoms, which gives:

$$\phi_{ij11} = \phi_{ij22} = \frac{2\theta}{N-1} \tag{5}$$

$$\phi_{ij12} = \phi_{ij21} = \frac{\pi}{2} - \frac{2\theta}{N-1} \tag{6}$$

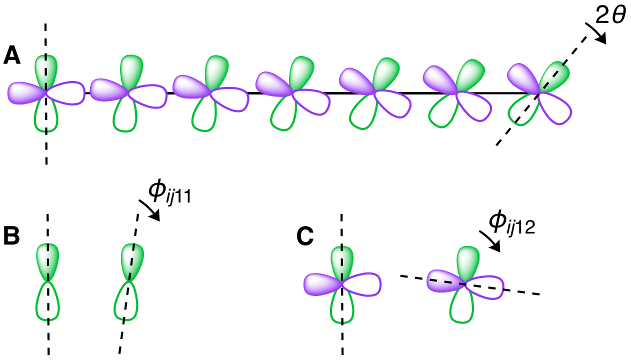

Figure S1. The helical orbital basis for linear carbon chains. (**A**) An angle of 2θ is accumulated over the chain length. (**B**) Angle between neighboring orbitals with $k = l$. (**C**) Overlap between neighboring orbitals with $k \neq l$.

Single-bond terminated carbon chains with an odd number of bonds tend to undergo a Peierls distortion towards a polyynic structure with bond length alternation (BLA), whereas double-bond terminated carbon chains with an even number of bonds tend to be cumulenic with all bonds equal in length. In closed-shell $C_{13}Cl_2$ as drawn in Fig. 2B there is a seven-bond segment ($N = 8$ including two sp^2-hybridized carbons), which we can expect to have BLA $\neq$ 0, and a six-bond segment ($N = 7$), in which we set BLA = 0. To evaluate the effect of BLA in the seven-bond segment (labelled 7bs), we assume it increases or decreases t_0 by a percentage δ (*62*):

$$t_{0,(7\mathrm{bs})} = t_0\left(1+(-1)^i\delta\right) \tag{9}$$

$$t_{0,(6\mathrm{bs})} = t_0 \tag{10}$$

To extend the conjugation through the whole ring, we add next-nearest-neighbor couplings between the sp-hybridized atoms (6 and 8; 13 and 2) on opposing sides of sp^2-hybridized atoms 7 and 1 (**fig. S2** and Fig. 2B in main text):

$$\hat{H}_{nnn} = -\sum_{\langle k,l\rangle}^{2} t_{6,8kl} c_{6k}^{\dagger} c_{8l} - \sum_{\langle k,l\rangle}^{2} t_{13,2kl} c_{13k}^{\dagger} c_{2l} \tag{11}$$

where the next-nearest-neighbor coupling values $t_{6,8kl}$ and $t_{13,2kl}$ depend on θ analogously to Eq. 2:

$$t_{6,8kl} = t_{nnn} \cos \phi_{6,8kl} \tag{12}$$

$$t_{13,2kl} = t_{nnn} \cos \phi_{13,2kl} \tag{13}$$

These approximations yield the Hamiltonian:

$$\hat{H} = \hat{H}_{nn}(t_0, \delta, \theta) + \hat{H}_{nnn}(t_{nnn}, \theta) \tag{14}$$

which depends on nearest-neighbor and next-nearest-neighbor couplings t_0 and t_{nnn}, the proportion of BLA δ in the seven-bond segment, and the tilt angle θ (**figs. S2A, S4**). Finally, out-of-plane bending of the sp^2-hybridized carbons can be added as:

$$\hat{H} = \hat{H}_{nn}(t_0, \delta, \theta) + \hat{H}_{nnn}(t_{nnn}, \theta) + 2\frac{1}{2}k_{\mathrm{bend}} \sin^2 \theta \tag{15}$$

where the final harmonic term is multiplied by two as bending occurs at atoms C1 and C7 (**fig. S2A**).

In the case of $\theta = 0$, we assume a Hückel GML^0_4 basis, with separate in-plane and out-of-plane π-systems (**fig. S2B**), and construct the tight-binding Hamiltonian using Eqs. 3, 4. For a finite value of θ we choose a half-Möbius GML^1_4 basis (**fig. S2C**). Similarly to the STM data and the obtained Dyson orbitals (see main text), this basis has a large (90° – 2θ) twist in the six-bond segment, and and a small 2θ twist in the seven-bond segment, and it is described by Eqs 5, 6.

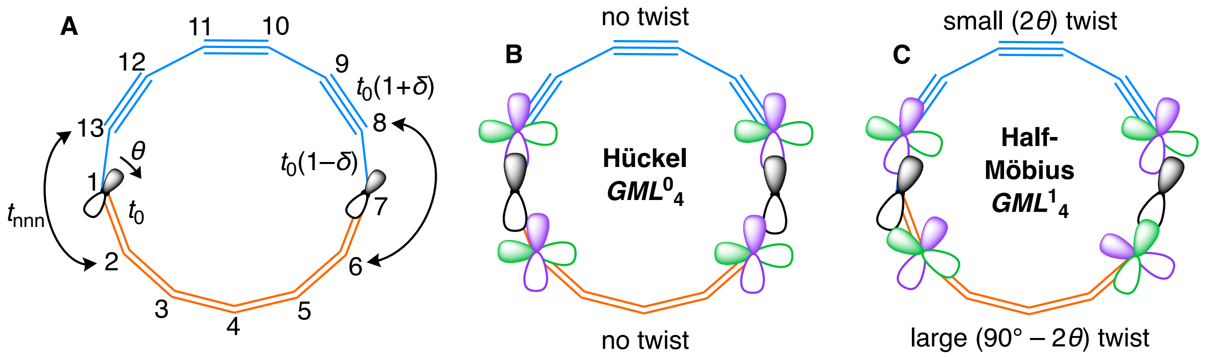

Figure S2. Tight-binding description (A) and possible bases (B, C) of $C_{13}Cl_2$. (**A**) Atom labelling and parameters of the tight-binding Hamiltonian for $C_{13}Cl_2$. The lone *p*-orbitals of sp^2-hybridized atoms 1 and 7 are shown. (**B, C**) Possible bases in which the tight-binding Hamiltonian can be evaluated.

To explore the variation of the energy with θ, we need to choose values of $t_0, t_{\mathrm{nnn}}, \delta$, and k_{bend}. Results are shown in **fig. S3**. Working in units of t_0, we use $t_{\mathrm{nnn}} = 0.1t_0$ and use $\delta = 0.0$ (no BLA, left column of **fig. S3**), $\delta = 0.1$ (moderate BLA, middle column of **fig. S3**) and $\delta = 0.2$ (strong BLA, right column of **fig. S3**). To explore bending, we choose $k_{\mathrm{bend}} = 0$ (first row of **fig. S3**), $k_{\mathrm{bend}} = t_0/2$ (middle row of **fig. S3**), and $k_{\mathrm{bend}} = t_0$ (third row of **fig. S3**).

In the case of the singlet (which has the twelve lowest MOs doubly occupied), we find that the combination of $\delta = 0.1$ and $k_{\mathrm{bend}} = t_0$, shown in **fig. S3H**, gives a good agreement with multireference calculations (**table S1** and shaded region of **fig. S3**).

For all explored values, the triplet (in which one electron is promoted from the HOMO to the LUMO, i.e. it is indistinguishable from the open-shell singlet) has an energy minimum at $\theta = 0$, in agreement with our multireference calculations (**table S1**).

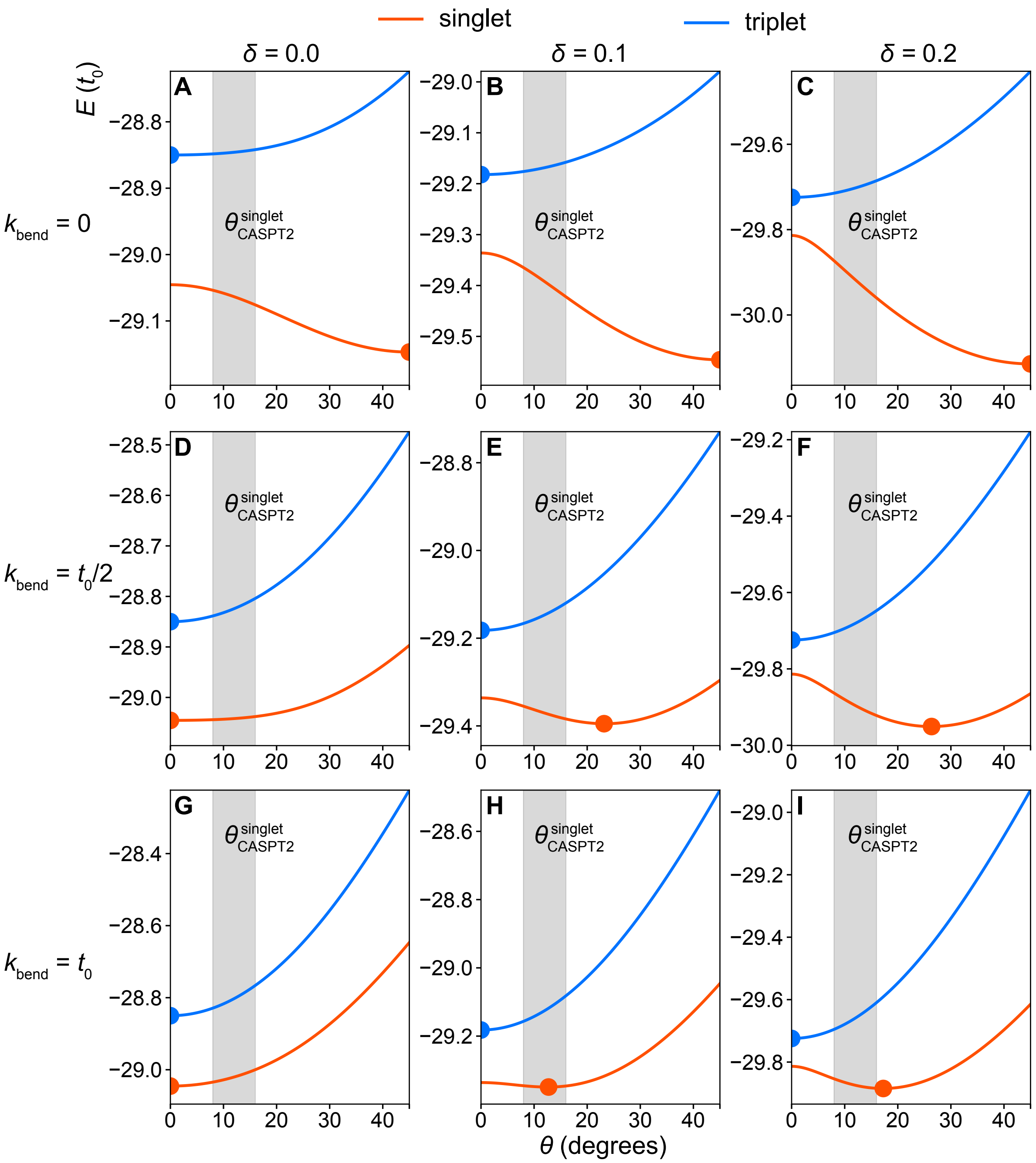

Figure S3. Tight-binding calculations of $C_{13}Cl_2$. Energies E in units of t_0 for different tilt angles θ obtained using Eq. 15. Singlet energies (orange) are the sum of twelve lowest MO energies multiplied by two. Triplet energies (blue) were obtained by promoting one spinless electron from the HOMO to the LUMO. As spin is not considered here, the results for the triplet also describe an open-shell singlet. In all cases we assume $t_{nnn} = 0.1t_0$, For BLA we consider $\delta = 0$ (first column, **A**, **D**, **G**), $\delta = 0.1$ (second column, **B**, **E**, **H**), $\delta = 0.2$ (third column, **C**, **F**, **I**), and for bending $k_{\text{bend}} = 0$ (first row, **A–C**), $k_{\text{bend}} = \frac{1}{2}t_0$ (second row, **D–F**), $k_{\text{bend}} = t_0$ (third column, **G–I**). The CASPT2-obtained value of θ is ~0° for the triplet state and 8–15° for the singlet, corresponding to the calculated values on NaCl (shaded in gray). The respective equilibrium geometry predicted by tight-binding is highlighted as a dot.

3.2. Multireference calculations

Geometry relaxations and Dyson orbital calculations were done using Molcas 24.02 (*63*). Geometries of $C_{13}Cl_2$ and $C_{13}H_2$ were relaxed in the singlet and triplet states at the CASPT2(12,12)/cc-pVDZ level of theory, that is 12 electrons in 12 orbitals. An IPEA shift of 0.25 a.u. was used. Analytical gradients (*64*) were computed in Cartesian coordinates, and relaxations were done using the quasi-Newton algorithm with a maximum step size of 0.05 a.u. until the gradient norm was below 0.01 a.u. and the energy in successive iterations oscillated by ~1 meV. $C_{13}H_2$ was only relaxed in the gas phase, while relaxations of $C_{13}Cl_2$ were done both in the gas phase and on-surface (see **fig. S5**). In the latter case, the surface was represented by a bilayer of point charges following the methodology established in our previous work (*22*). Geometric parameters of optimized $C_{13}Cl_2$ and $C_{13}H_2$ are compared in **Table S1**.

Dyson orbitals were computed by using the state interaction method (*65*) from MS-CASPT2 calculations with three roots for the –3, –2, –1, 0, +1, +2, and +3 charge states, done at the on-surface optimized singlet and triplet geometry of the neutral state. The ionization potentials and electron affinities obtained this way are shown in **Table S2**. The spin-orbit coupling matrix element between the singlet and triplet state was calculated at the CASSCF(12,12)/ANO-RCC-VTZP level of theory using the state-interaction method.

Optimized CASPT2 geometries and Dyson orbital cube files are available at (*59*) 10.5281/zenodo.15495263.

Nucleus-independent chemical shift (NICS) calculations were done using the development version of Dalton 2025 (*66*) at the CASSCF(12,12)/cc-pVDZ level of theory.

Table S1. Tilt (θ_1 and θ_2) and twist ($\varphi = \theta_1 + \theta_2$) angles of $C_{13}Cl_2$ and $C_{13}H_2$, estimated as an angle between the C–X (X = Cl or H) bond and the average plane defined by sp-hybridized atoms (see **fig. S4**), based on CASPT2(12,12)-optimized geometries.

	θ_1	θ_2	φ
^{1}**2** (NaCl)	15.2	9.5	24.7
^{1}**2** (gas)	15.8	8.5	24.3
singlet $C_{13}H_2$ (gas)	19.9	20.4	40.2
^{3}**2** (NaCl)	–1.6	3.6	2.0
^{3}**2** (gas)	0.2	1.0	1.2
triplet $C_{13}H_2$ (gas)	3.0	2.6	5.6

Table S2. First three ionization potentials (IP) and electron affinities (EAs) in eV, as calculated at the MS-CASPT2(12,x)/ANO-RCC-VTZP, x = 9–15, level of theory on the CASPT2(12,12)/cc-pVDZ optimized geometries of the neutral singlet and triplet.

	^{1}**2**	^{3}**2**
IP3	35.5	34.7
IP2	19.3	18.9
IP1	7.8	7.2
EA1	2.1	2.5
EA2	0.1	0.9
EA3	–7.0	–6.4

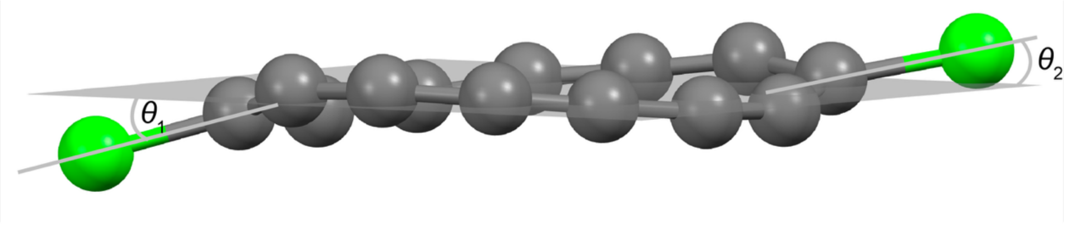

Figure S4. Definition of tilt angles. The plane is fit through all sp-hybridised atoms. The twist angle φ corresponds to the sum of the tilt angles θ_1 and θ_2, i.e., $\varphi = \theta_1 + \theta_2$.

3.3. Aromaticity

The change in topology from trivial to helical is also reflected in the aromaticity of **2**. The NICS trends are similar on the surface and in the gas phase (see **fig. S5**). As the weak interactions with the surface are not immediately relevant to our analysis, we shall focus on the gas-phase structures.

In the planar triplet minimum, ^{3}**2** has roughly 13 electrons in the out-of-plane and 11 electrons in the in-plane π-system and the major contribution to its wavefunction is the $^3|11>$ configuration. Such an electronic structure results in both diatropic and paratropic contributions to the induced current (*22, 62*) and results in overall anti-aromaticity, with NICS(2)$_{zz}$ = 6.2 ppm. The planar singlet ^{1}**2**$_{\textbf{@triplet}}$, which has helical natural orbitals and a dominant $^1|11>$ contribution, is less anti-aromatic (NICS(2)$_{zz}$ = 3.3 ppm) than ^{3}**2**. This anti-aromaticity relief can be attributed to the contribution of closed-shell configurations |20> and |02>, as relaxing the singlet into its non-planar minima ^{1}**2-M** or ^{1}**2-P** (described as |20> and |02>, respectively) results in further anti-aromaticity relief, with NICS(2)$_{zz}$ = –3.7 ppm. This $C_s \rightarrow C_1$ symmetry-breaking is highly analogous to the pseudo-Jahn–Teller $D_{4h} \rightarrow D_{2h}$ distortion in cyclobutadiene (*32*), which is also accompanied by anti-aromaticity relief.

A defining characteristic of the non-planar singlets ^{1}**2-M** and ^{1}**2-P** is the mixing of the in-plane and out-of-plane π-systems of the carbon ring into a single 24-electron helical π-system. Their weak aromaticity (or weak anti-aromaticity for the on-surface geometry) can be rationalized by noting that their orbital basis has the topology of a $GML^{\pm1}{}_4$ body. This means that they do not follow rules for Hückel aromaticity (valid for $GML^0{}_{2h}$ bodies, h is an integer), which would imply strong anti-aromaticity for 24 (4n) electrons. They also do not closely follow the rules for conventional Möbius aromaticity (valid for $GML^h{}_{2h}$ bodies), as those would imply strong aromaticity for 24 electrons. Moreover, the non-planar triplet ^{3}**2**$_{\textbf{@singlet}}$ displays very similar NICS values to the singlet minima, suggesting that Baird's rule, which is valid both for Hückel and Möbius systems (*67*), may not apply here, possibly related to a change of topology. While further investigation of half-Möbius aromaticity is needed, our results suggest that both diatropic and paratropic contributions to the ring current are present, as the obtained NICS values appear to be highly sensitive to geometry (*62*), see **fig. S5**.

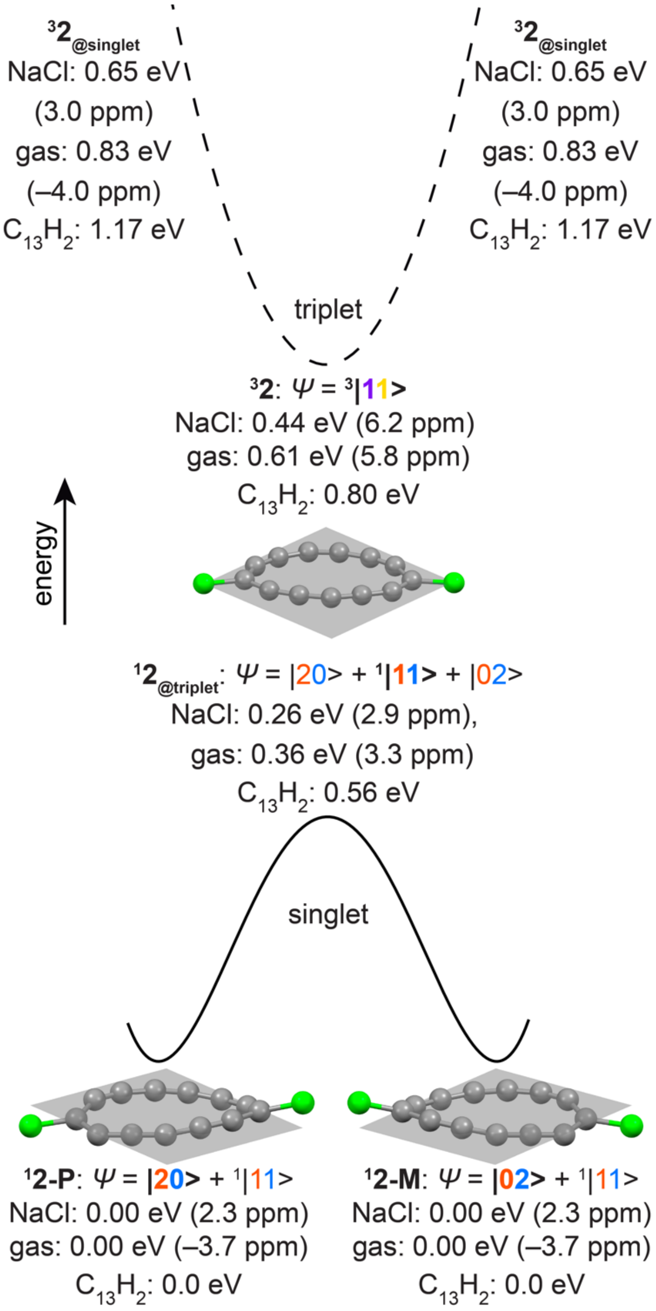

Figure S5. Multireference calculations of $C_{13}Cl_2$ on the surface and in the gas phase, and $C_{13}H_2$ in the gas phase. Energy diagram, with energies in eV, for the singlet ^{1}**2** , and the triplet ^{3}**2**. C atoms are shown in gray and Cl atoms in green. NICS(2)$_{zz}$ values in ppm for $C_{13}Cl_2$ gas-phase geometries are shown in parentheses. ^{1}**2**$_{\textbf{@triplet}}$ is the singlet in the equilibrium geometry of ^{3}**2**, and ^{3}**2**$_{\textbf{@singlet}}$ is the triplet in the equilibrium geometry of the singlet. Multireference states are described by configurations that contribute significantly to their composition, with dominant contributions shown in bold.

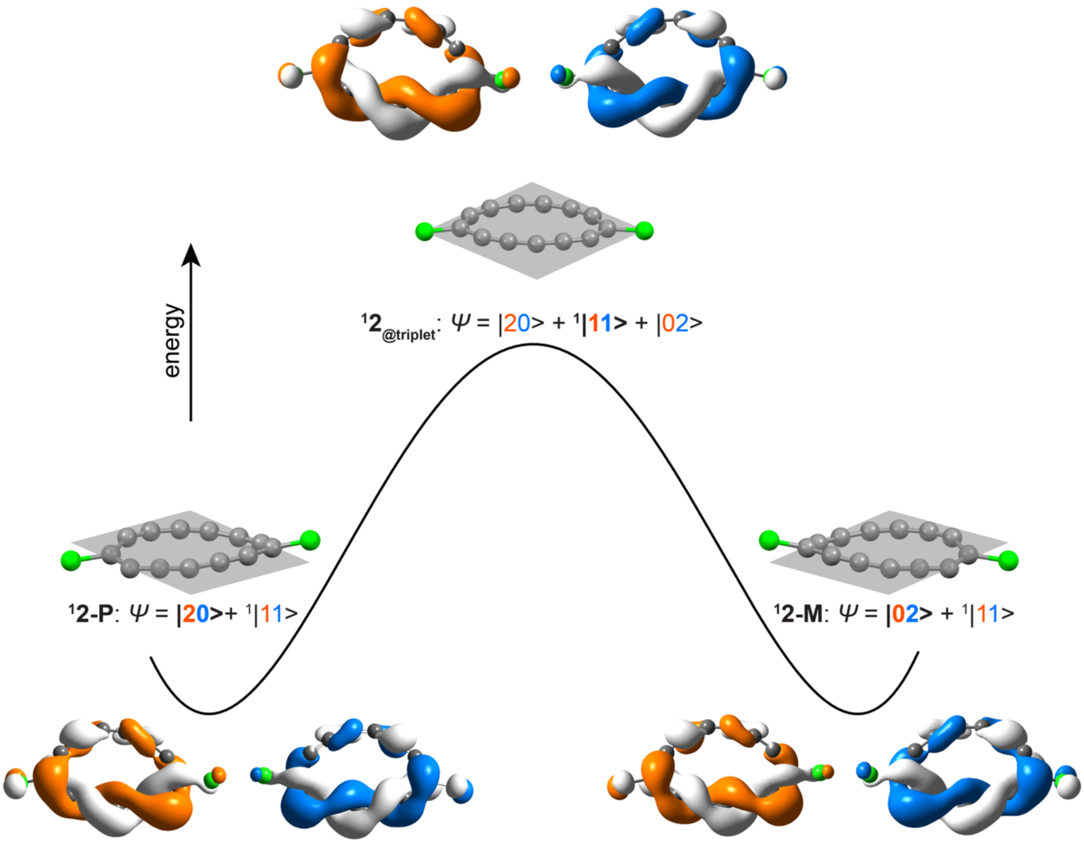

Figure S6. Natural frontier orbitals of ^{1}2 in different geometries. Natural orbitals are shown for geometries calculated in the gas phase. ^{1}**2**$_{\textbf{@triplet}}$ denotes the singlet in the equilibrium geometry of ^{3}**2**. Dominant contributions to the wavefunction are shown in bold. The natural occupations of the orange and blue orbital in ^{1}**2**$_{\textbf{@triplet}}$ (same as shown in Fig. 3C) are 0.97 and 1.02, respectively. As the triplet geometry is not perfectly planar, see **Table S1**, these two populations are not exactly equal, and the orange and blue orbitals are not exact mirror images of each other. For the relaxed gas phase geometry of the singlet ^{1}**2-P** (^{1}**2-M**), the occupations of the orange and blue orbitals are 1.5 and 0.5 (0.5 and 1.5), respectively. The structures and natural orbitals of ^{1}**2-P** are mirror symmetric with respect to those of ^{1}**2-M**, e.g., the HOMO of ^{1}**2-P** (colored orange) is mirror symmetric to the HOMO of ^{1}**2-M** (colored blue). The natural occupations of the triplet, shown in Fig. 3B are 0.95 and 0.96 for the purple and yellow orbital, respectively.

3.4. DFT calculations of $C_{12}Cl_2$*,* $C_{13}Cl_2$*, and* $C_{14}Cl_2$

The range-separated ωB97X-D functional (*68*) qualitatively reproduces the CASPT2-optimized singlet geometry of $C_{13}Cl_2$ well. We used the ωB97X-D/def2-SVP level of theory to compare equilibrium singlet geometries of $C_{12}Cl_2$ (two six-bond segments), ^{1}**2** (i.e., $C_{13}Cl_2$, six- and seven-bond segment), and $C_{14}Cl_2$ (two seven-bond segments). DFT predicts that ^{1}**2** is non-planar and that $C_{12}Cl_2$ and $C_{12}Cl_2$ singlets are planar, see **Table S3**. These calculations were done using Gaussian16 (*69*).

Table S3. Tilt (θ_1 and θ_2) and twist ($\varphi = \theta_1 + \theta_2$) angles, see **fig. S4** for definition, of optimized geometries of singlet $C_{13}Cl_2$, ^{1}**2** ($C_{13}Cl_2$) and $C_{14}Cl_2$, estimated as an angle between the C–X (Cl or H) bond and the average plane defined by sp-hybridized atoms. In all three DFT-investiated systems, frequency calculations confirmed that the obtained geometries were minima.

	θ_1	θ_2	φ
^{1}**2** (gas, CASPT2	8.5	15.8	24.3
^{1}**2** (gas, ωB97X-D)	18.6	18.7	37.3
$C_{12}Cl_2$ (gas, ωB97X-D)	0.0	0.0	0.0
$C_{14}Cl_2$ (gas, ωB97X-D)	0.0	0.0	0.0

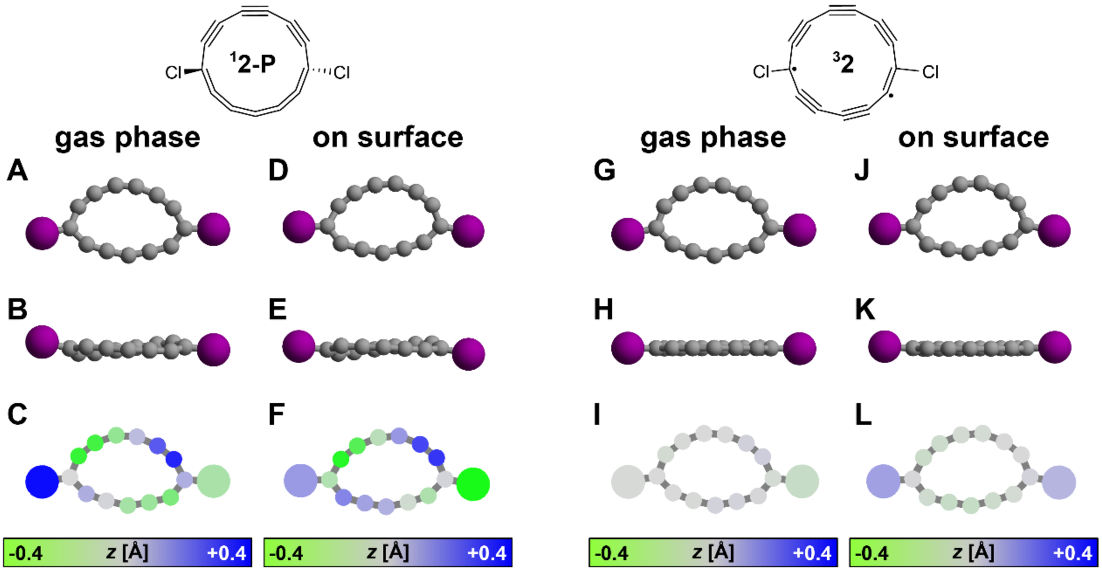

Figure S7. CASPT2-optimized geometries. CASPT2(12,12) calculated geometries of ^{1}**2-P** and ^{3}**2** in the gas phase and on NaCl. The bottom row shows the distortion with respect to the average plane of the nuclei of the molecule. Representations of the on-surface calculations that display also the NaCl substrate are shown in **figs. S14** and **S15**.

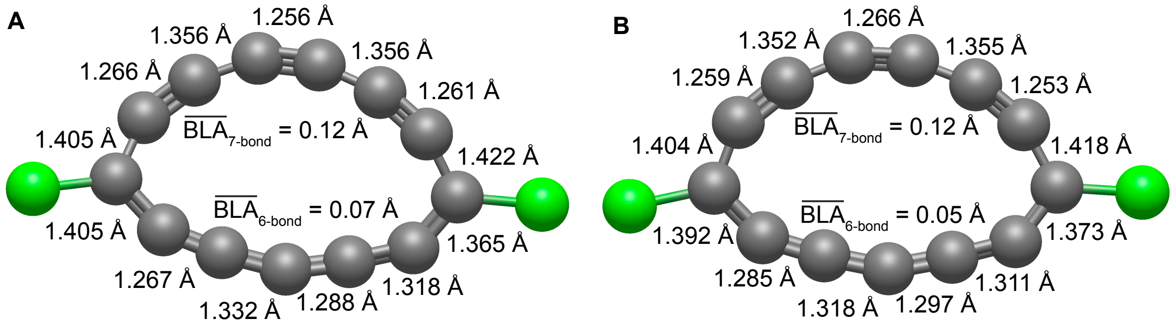

Figure S8. Bond lengths in CASPT2-optimized on-surface geometries of $C_{13}C_2$ in the singlet (A) and triplet (B) state. Average values of bond-length alternation (BLA) for the seven- and six-bond segments are shown (for the latter, the lower rightmost bond is not included in the average, because bond length is not alternating for this bond of the six-bond segment). For reference, the multireference results for cyclo[16] carbon predict a BLA value of ~0.12 Å (*44*), while coupled clusters results for cyclo[18]carbon predict a BLA of ~0.14 Å (*70*). Note that in the closed-shell Lewis structure of the singlet, see Fig. 2B, the seven-bond segment is drawn as a polyyne and the six-bond segment as a cumulene. The CASPT2-optimized geometry somewhat validates this structure, as the bond-length alternation in the seven-bond segment is similar to that in polyynes. However, we also find some bond-length alternation in the six-bond segment and irregular bond-length alternation through the seven-bond segment.

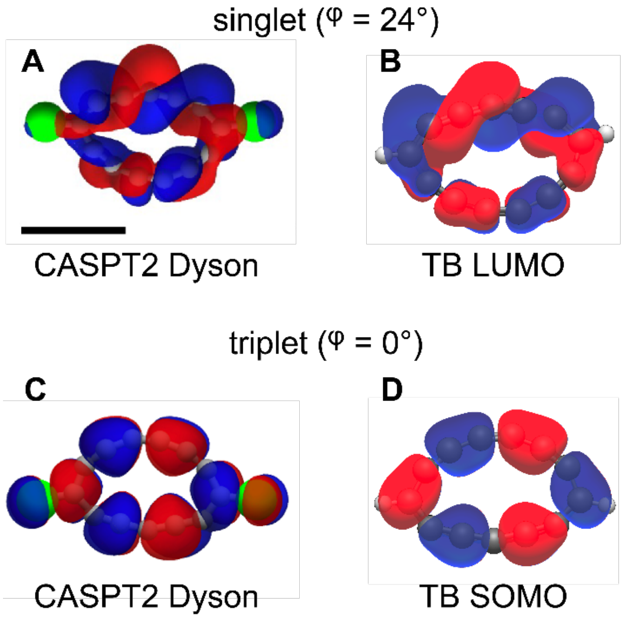

Figure S9. Electron attachment to ^{1}2 (A,B) and detachment from ^{3}2 (C,D). (**A**) Dyson orbital for electron attachment to the geometry-optimized $C_{13}Cl_2$ singlet calculated using CASPT2. (**B**) LUMO obtained using the tight-binding model and the half-Möbius topology GML^1_4, see **fig. S2C**. (**C**) Dyson orbital for electron detachment from the geometry optimized $C_{13}Cl_2$ triplet calculated using CASPT2. (**D**) The energetically lower SOMO obtained using the tight-binding model and the Hückel GML^0_4 topology, see **fig. S2B** (the higher SOMO is in-plane and therefore will result only in very weak contrast in STM (*22*)). Tight-binding parameters used are $t_{nnn} = 0.1t_0$, $\delta = 0.1$, (orbitals do not depend on k_{bend}). The disagreement at sp^2-hybridized atoms 1 and 7 is explained by our tight-binding model not considering their substituents.

3.5. Quantum calculations

The recently-proposed SqDRIFT quantum algorithm (*36*) is a quantum-computing counterpart of classical selected Configuration Interaction approaches (*71*). These approaches rely on the observation that, even in strongly-correlated systems, the exact full-configuration interaction wave function has a non-negligible support over an array of determinants, which can be written as $\{|\sigma_i^{\text{SCI}}\rangle\}$, that is dramatically smaller than the full determinant space. SqDRIFT leverages the quantum computer as a sampling machine to construct the $\{|\sigma_i^{SCI}\rangle\}$ space.

Among the different sample-based quantum diagonalization variants, in SqDRIFT the quantum circuits used for the sampling phase are constructed as time-evolution circuits, i.e.

$$|\psi\rangle = e^{-iHt}|\psi_0\rangle \ , \qquad (16)$$

where $|\psi_0\rangle$ is a reference determinant (here taken as the lowest-energy closed-shell configuration), and H is the electronic Hamiltonian, which we decompose as sum of elementary Fermionic operators h_i as:

$$H = \sum_i c_i \, h_i \qquad (17)$$

The time-evolution operator is randomized through the qDRIFT protocol (*72*) as

$$e^{-iHt} \approx \prod_k e^{-ih_k t} \tag{18}$$

where the product includes only a subset of all the h_k terms, sampled according to a probability distribution proportional to $|c_k|^2$. In practice, multiple randomized approximations are generated and executed on the quantum processors. This randomized compilation step enables a dramatic reduction of the circuit depth, making it feasible to utilise SqDRIFT on current quantum processors to solve complex quantum-chemical problems.

The parameters to be set in an SqDRIFT simulation are the following:

1. The number of randomized approximations of the time-evolution operator that are executed as quantum circuits. Each randomized approximation is constructed from Eq. 18, sampling a different subset of terms h_k that are included in the product.
2. The number of Hamiltonian terms h_k to be included in the time-evolution circuit for each randomization.
3. The number of samples to be collected from each circuit.
4. The dimension of the subspace in which the Hamiltonian is diagonalized.

Among the different sample-based quantum diagonalization approaches proposed in the literature, SqDRIFT is particularly appealing because it has been proven that sampling from the circuits defined above yields the $\{|\sigma_i^{\mathrm{SCI}}\rangle\}$ array with high probability (*36*). This is strictly true only when a large number of terms h_k relative to the Hamiltonian norm $\sum_i |c_i^2|^2$ is included in each approximate time-evolution circuit. However, it has been empirically observed the relevant determinants $\{|\sigma_i^{\mathrm{SCI}}\rangle\}$ are already identified through sampling from relatively shallow circuits (*36*). In practice, the number of samples should be large enough to ensure that all configurations contributing to the ground-state wave function are included in the subsequent diagonalization step.

In addition to SqDRIFT, we also executed quantum calculations using the extended SqDRIFT (ext-SqDRIFT) (*73*) approach. Ext-SqDRIFT first executes an SqDRIFT calculation and diagonalizes the Hamiltonian in the resulting determinant space. A second subspace is then constructed including the determinants for which $|c_i| > \eta$ (with $\eta = 10^{-3}$ for the neutral species and $5 \cdot 10^{-4}$ for the anionic one) are retained. In an analogy with multireference CISD, this subspace is then extended by including all possible single (S) and double (D) excitations constructed starting from the existing ones. The Hamiltonian is then classically diagonalized in the resulting subspace.

To explore an active space beyond the reach of conventional approaches, we performed SqDRIFT calculations on an IBM quantum processor (see below for additional details on the quantum hardware) carried out on an active space of 32 electrons in 36 orbitals for the neutral molecular system, and 33 electrons in 36 orbitals for the anionic molecular system. Such an active space includes all carbon π electrons and per chlorine four electrons that mix with the π-system of $C_{13}Cl_2$. The molecular orbitals were obtained from a smaller-scale CASSCF calculation, based on an active space including 12 electrons in 12 orbitals. The resulting Hamiltonian consists of a total of 222814 fermionic second-quantization operators.

To execute SqDRIFT on a quantum processor, the molecular Hamiltonian had to be mapped onto the quantum hardware. This was performed using Jordan-Wigner mapping (*74*), which resulted in 72-qubit circuits. For a system of this size, full implementation of Trotterized time evolution (*75*) would be impractical on current quantum hardware. Even a circuit specifically designed for near-term quantum devices, such as the Local Unitary Cluster Jastrow ansatz (*76*), would result in a final two-qubit circuit depth of 286, exceeding the capabilities of current hardware.

To sidestep these limitations, we employed the qDRIFT protocol, which randomizes the Hamiltonian terms to be implemented within the quantum circuit, effectively reducing the circuit depth. For each molecular system, several experiments are conducted using different numbers of sampled excitations and evolution times. Specifically:

- For each molecular system, circuits with 5, 10, and 15 fermionic excitations, constructed on top of the lowest-energy determinant obtained from the CASSCF orbitals, were considered;
- For each excitation count, circuits were prepared with three different evolution times, $t = 1,2,3$ (in atomic units);
- For each combination of excitation count and evolution time, 500 randomizations were executed.

This resulted in 1500 circuits per excitation count and a total of 4500 circuits per molecule. Each circuit was sampled 1024 times, yielding approximately 4.6 million samples per molecular system. The circuits were executed on *ibm_kingston*, a chip belonging to the second revision of IBM's Heron family of quantum processors.

The *ibm_kingston* quantum processor features 156 qubits, a median two-qubit gate error of $2.1 \cdot 10^{-3}$, and a median readout error of $8.5 \cdot 10^{-3}$. In the experiments, hardware noise was mitigated by discarding quantum samples that exhibited an incorrect particle number. Finally, the collected quantum samples were used to define the subspace in which the fermionic Hamiltonian was projected and diagonalized classically. Each Hamiltonian diagonalization was performed on a cluster composed of bare metal nodes consisting on four sockets each with a Intel Xeon Platinum 8260 (2.40 GHz) processor, for a total of 196 cores. The dimension of the subspace was adjusted by increasing the size of the batch of quantum samples considered. The reported calculations were obtained with batch sizes ranging from 500 to 5000 samples, leading to Hilbert subspaces including up to 20 million determinants. Using up to 30 cores of the aforementioned cluster, the largest diagonalizations required approximately 10 minutes. Results of the SqDRIFT calculations, showing the energy of ^{1}**2** and its anion as a function of the subspace diagonalization dimension are presented in **fig. S10**

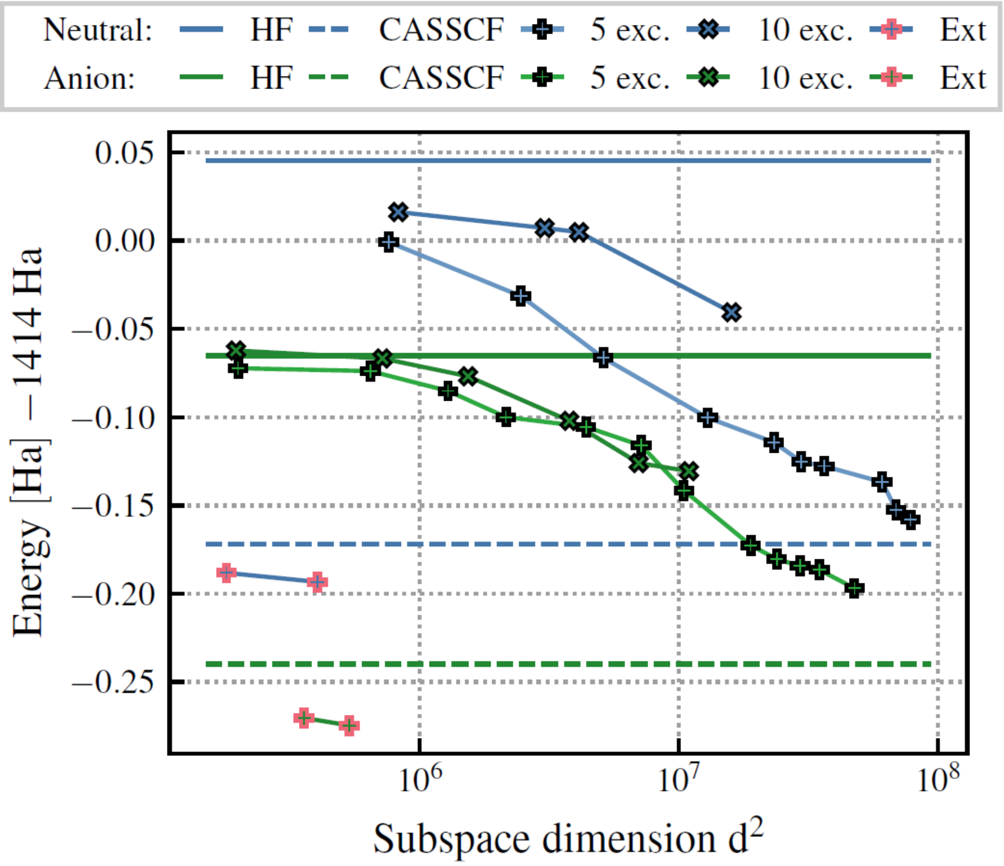

Figure S10. Energy of the neutral and anion as a function of the subspace diagonalization dimension. The Hartree-Fock (HF) energies serve as references and are reported in the solid lines at −38475.67 eV and −38478.69 eV for the neutral ^{1}**2** (neu) and anion (ani) of **2**, respectively. The SqDRIFT energies obtained using 5 and 10 excitations (exc.) for the neutral ^{1}**2** (shades of blue; min: −38481.24 eV for 5 exc.) and the anion of **2** (shades of green; min: −38482.29 eV for 5 exc.), respectively. Ext-SqDRIFT energies are also reported (red crosses; neu: −38482.192 eV, ani: −38484.405 eV).

As described above, SqDRIFT leverages the quantum processor solely as a sampling machine, and the subsequent diagonalization is executed classically. This means that classical representations of the neutral and charged (anionic) wave function are available, given as:

$$|\Psi_{\text{neutral}}\rangle = \sum_{i \in S_{\text{neutral}}} c_i^{\text{neutral}} |\sigma_i^{\text{neutral}}\rangle, \tag{19}$$

and

$$|\Psi_{\text{anionic}}\rangle = \sum_{i \in S_{\text{anionic}}} c_i^{\text{anionic}} |\sigma_i^{\text{anionic}}\rangle. \tag{20}$$

$S_{neutral}$ and $S_{anionic}$ are the subspaces sampled by SqDRIFT for the neutral-state and anionic-state wave functions, respectively. $\sigma_i^{neutral}$ and $\sigma_i^{anionic}$ are Slater determinants constructed from the molecular orbitals of the neutral and anionic species, respectively. Following our previous work (*22*), we expand the Dyson orbital in terms of the ground-state wave function molecular orbitals as:

$$\psi_{Dyson}(\boldsymbol{r}) = \sum_{\mu} d_{\mu} \phi_{\mu}(\boldsymbol{r}), \tag{21}$$

and calculate the expansion coefficient as:

$$d_{\mu} = \langle a_{\mu}^{\dagger} \Psi_{\text{neutral}} | \Psi_{\text{anion}} \rangle. \tag{22}$$

The coefficient is calculated, in practice, by expressing the correlated wave functions $|\Psi_{\text{neutral}}\rangle$ and $|\Psi_{\text{anionic}}\rangle$ according to their definition, obtaining:

$$d_{\mu} = \sum_{i,j} \left(C_i^{\text{neutral}} \right)^{\star} C_j^{\text{anionic}} \langle a_{\mu}^{\dagger} \sigma_i^{\text{neutral}} | \sigma_j^{\text{anionic}} \rangle. \tag{23}$$

The determinants $|a_{\mu}^{\dagger} \sigma_i^{\text{neutral}}\rangle$ and $|\sigma_j^{\text{anionic}}\rangle$ are expressed in terms of their respective CASSCF-optimised orbitals, which are however obtained from the same basis set. Hence, the overlaps appearing in the expression for d_{μ} can be calculated using standard strategies borrowed from non-orthogonal configuration interaction. Note that we accelerated the calculation of the Dyson orbital by neglecting, in the last equation, coefficients with a magnitude smaller, in absolute value, than 0.001 (this truncation has negligible impact on the Dyson orbital).

The thus obtained Dyson orbital for electron attachment to **^{1}2**, based on the SqDRIFT calculation, is shown in the main text in Fig. 3D, left panel. The SqDRIFT calculations used for both the neutral and anionic wave functions were run including 5 excitations per circuit. The subspace dimension d^2 used for the classical diagonalization is the largest amongst the ones reported in **fig. S10**. The Dyon orbital obtained by SqDRIFT agrees well with the the classical calculations using CASSCF in an active space of 12 correlated electrons shown in Fig. 3D, right panel (see also **fig. S9A** for the Dyson orbital calculated using CASPT2) indicating that the active space of 12 correlated electrons is sufficient to describe the system well.

4. Additional data and analyses

4.1. Different isomers of $C_{13}Cl_2$

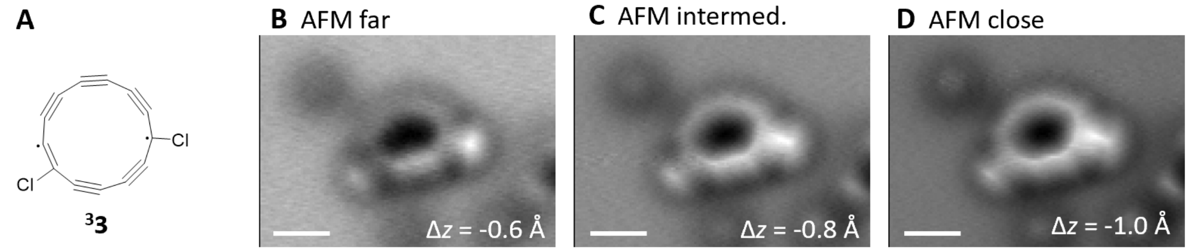

Figure S11. $C_{13}Cl_2$ isomer 3. (**A**) Resonance structure of ^{3}**3**. (**B–D**) AFM data on monolayer NaCl (setpoint $I = 0.5$ pA, $V = 0.2$ V; Δz as indicated). The AFM data indicates a planar ring geometry and thus points towards a triplet state ^{3}**3**. Δf scales from black to white, B [-6.2 Hz; -0.5 Hz], C [-6.7 Hz; +1.4 Hz], D [-6.5 Hz; +2.9 Hz]. All scale bars 5 Å.

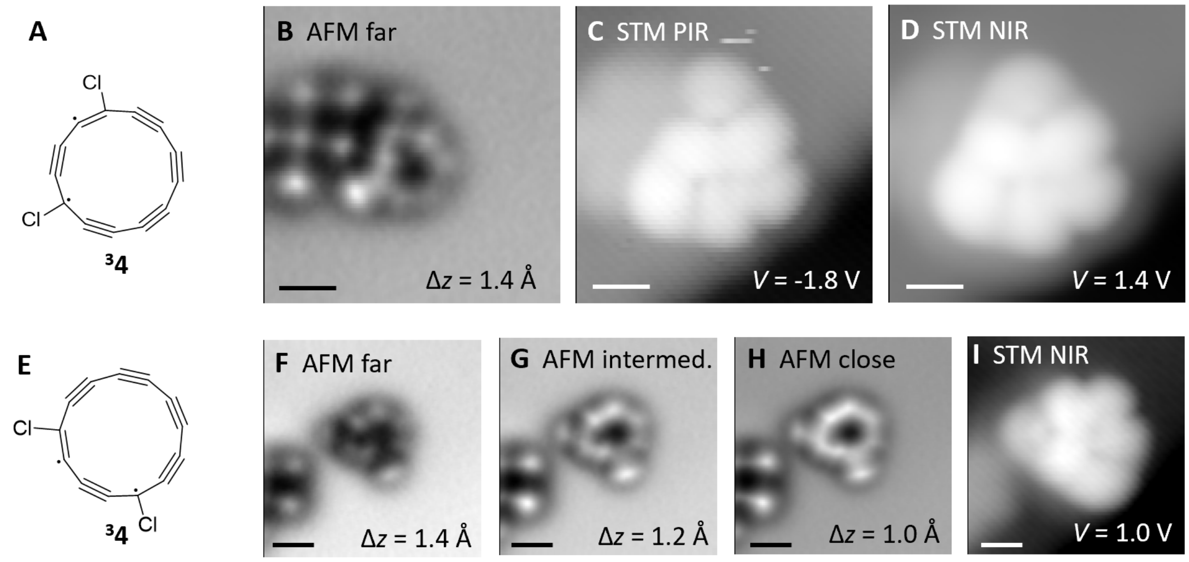

Figure S12. $C_{13}Cl_2$ isomer 4. (**A**) and (**E**) resonance structures of the planar, triplet ^{3}**4**. (**B**) AFM data on bilayer NaCl near several Cl adatoms (setpoint $I = 0.6$ pA, $V = 0.2$ V; $\Delta z = 1.4$ Å) revealing a planar geometry of the ring. (**C**) STM at the PIR at $V = -1.8$ V, $I = 0.4$ pA. (**D**) STM at the NIR at $V = 1.4$ V, $I = 0.8$ pA. (**F–H**) AFM data of ^{3}**4** at an adsorption site further away from the Cl adatoms (setpoint $I = 0.6$ pA, $V = 0.2$ mV; Δz as indicated). (**I**) STM at the NIR at $V = 1.4$ V, $I = 0.8$ pA. Scales from black to white, B [-3.9 Hz; +1.8 Hz], C [0 Å; +5.7 Å], D [0 Å; +6.0 Å], F [-3.3 Hz; +0.2 Hz], G [-4.2 Hz; +0.8 Hz], H [-4.6 Hz; +2.6 Hz], I [0 Å; +6.4 Å]. All scale bars 5 Å. The open-shell character of ^{3}**4** is evidenced by the similarity of the PIR and NIR orbital-density images measured, see (C) and (D). PIR and NIR correspond to the singly occupied molecular orbital (SOMO) and singly unoccupied molecular orbital (SUMO) of the out-of-plane π-system, respectively (*77*). It is the same individual compound as in Fig. 6, A to D, however, after the bonding positions of the Cl atoms were manipulated (*22*) by applied voltage pulses. The molecule is adsorbed on bilayer NaCl, near a cluster of Cl adatoms.

4.2. Adsorption geometries

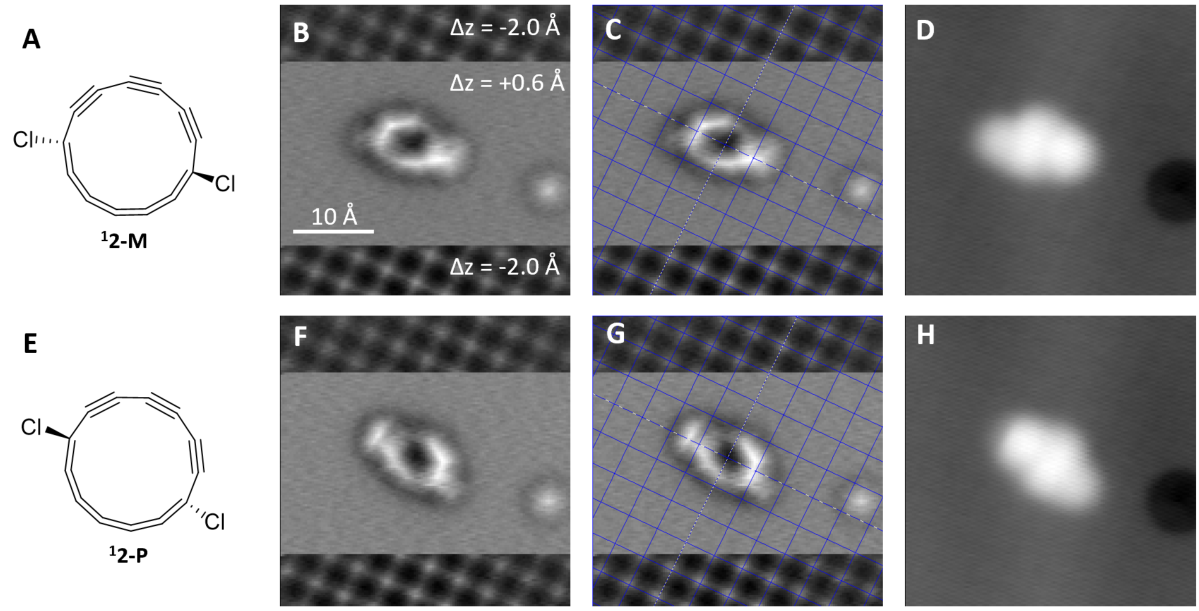

Figure S13. Experimental adsorption-site determination of ^{1}2-M and ^{1}2-P. (**A**) Lewis structure of ^{1}**2-M**. (**B**) AFM data of ^{1}**2-M** on bilayer NaCl on Au(111). The tip-height offset Δz was different in the top (Δz = -2.0 Å), center (Δz = 0.6 Å) and bottom (Δz = -2.0 Å) part of the image to resolve the substrate in top and bottom part and the molecule in the central part of the image (*41*). Setpoint V = 0.15 V, I = 0.4 pA. (**C**) Same data as in (B) with a grid overlaid, which vertices correspond to Cl sites of the NaCl surface. CO is adsorbed on a Na site. (**D**) STM of ^{1}**2-M**, V = 0.15 V, I = 0.4 pA. (**E**-**H**) Corresponding data for ^{1}**2-P**, after molecule had been switched from ^{1}**2-M** to ^{1}**2-P**. Scale bar 10 Å, applies to all measurements.

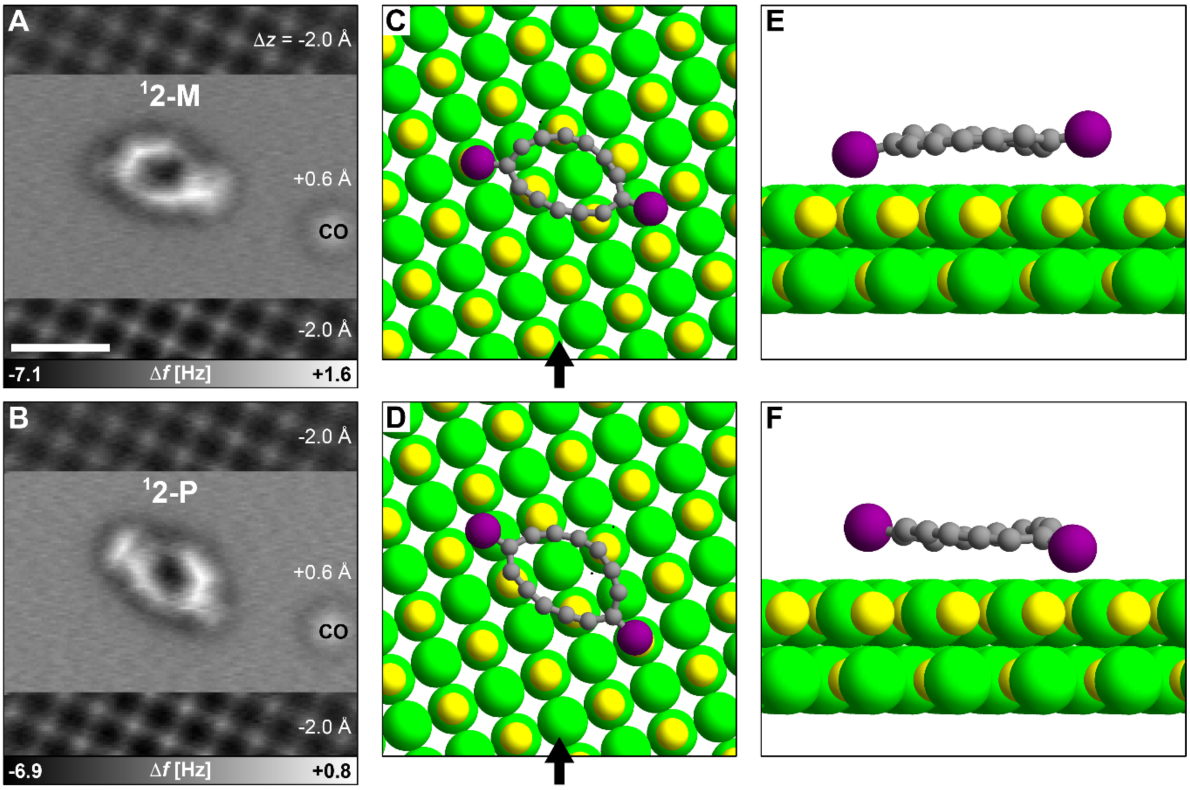

Figure S14. Comparison of adsorption geometry of ^{1}2-M and ^{1}2-P, experiment and theory. (**A, B**) AFM data to determine experimentally the adsorption site of ^{1}**2-M** and ^{1}**2-P**, respectively (see **fig. S13)**. Scale bar 10 Å. (**C, D**) Calculated relaxed adsorption geometries of ^{1}**2-M** and ^{1}**2-P**, respectively, on NaCl. Viewed from top, with the substrate oriented as in the experiment (A, B). Na cations in yellow and Cl anions of the NaCl surface in green; C atoms in gray and Cl atoms of the molecule in purple. (**E, F**) Side view along the direction of the arrows in (C, D), respectively. The theory reproduces the experiment very well, agreeing in adsorption site and adsorption orientation, comparing (A) with (C) and (B) with (D), and in the out-of-plane distortions of the molecule. Note that atoms that show a larger separation to the surface appear with brighter contrast in the AFM images (*41*), comparing (A) with (E) and (B) with (F). See also the corresponding AFM simulations using the Probe-Particle Model (*39*) in Fig. 4, D to F of the main text.

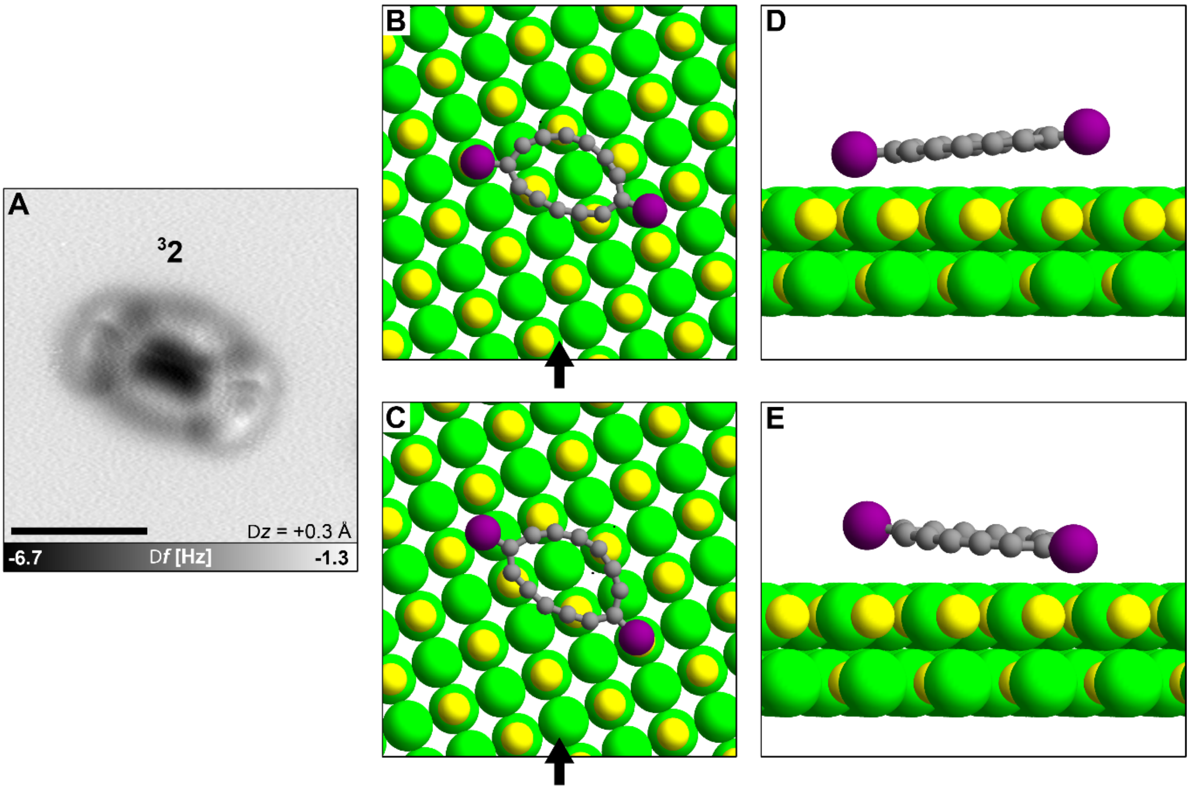

Figure S15. Adsorption geometry of ^{3}2. (**A**) AFM data at $V = 0.34$ V, setpoint $V = 150$ mV, $I = 0.2$ pA, $\Delta z = 0.3$ Å. Scale bar 10 Å. At this elevated voltage, the molecule is switching between different states at a faster rate than the bandwidth of the AFM (see Fig. 6 for measurements at adsorption sites that stabilized ^{3}**2**). In AFM images at $V = 0$ V the molecule on defect free NaCl was not stabilized in the open-shell state and thus not observed in the ^{3}**2** state and was always imaged in the states of either ^{1}**2-M** or ^{1}**2-P** (see **fig. S13**). The AFM image at 0.34 V (A) and the STM images at voltages >300 mV (**fig. S18**) show a twofold symmetry. The two-fold symmetry, the faint sharp lines and the multiple appearance of the Cl atoms at different locations in the AFM image (A) are indicative for a change of adsorption geometries, due to the interaction with the tip (*77*). (**B, C**) Calculated relaxed adsorption geometries of ^{3}**2** on NaCl. Viewed from top, with the substrate oriented as in the experiment (A). Na cations in yellow and Cl anions of the NaCl surface in green; C atoms in gray and Cl atoms of **2** in purple. (**D, E**) Side view along the direction of the arrows in (B, C), respectively. For ^{3}**2**, calculations reveal two prochiral adsorption sites (B, C). Note that even considering ^{3}**2** being planar, the system becomes prochiral upon adsorption. The adsorption sites and orientations in the two prochiral adsorption geometries of ^{3}**2** are similar to ^{3}**2-P** and ^{3}**2-M**, but the molecular geometry (out-of-plane distortions) is not. We assume that the AFM image (A) is affected by the molecule switching at a fast rate between four adsorption geometries: That of ^{1}**2-P** and ^{1}**2-M**, and of the two prochiral adsorption geometries of ^{3}**2**. The *I*(*t*) data (Fig. 5 and **figs. S21** and **S22**) suggest that at such conditions the ^{3}**2** state has a longer lifetime than ^{3}**2-P** and ^{3}**2-M**. Therefore, we assume that under these conditions the molecule is most of the time in the ^{3}**2** state. The AFM image in (A) seems in-line with a superposition of the two calculated adsorption geometries of ^{3}**2**. However, because of the four states involved, and the switching being fast compared to the AFM and STM bandwidth, such images are challenging to simulate and interpret (*77*). Moreover, we assume that the relative lifetimes of all four states depend on the vertical and lateral tip position. Depending on the tip position, one of the two adsorption geometries of ^{3}**2** might be preferred and/or fast switching between the two adsorption geometries of ^{3}**2** might be possible, which might be reasons for the observation of only one current plateau for the ^{3}**2** state in $I(t)$ data (see **figs. S19**, **S20**, **S23** and **S24**). Stable AFM images of ^{3}**2** were obtained near defects, see Fig. 6, A and D and **fig. S17**, agreeing well with the calculated adsorption geometry of ^{3}**2** being planar, but adsorbed non-parallel with respect to the NaCl surface, see (B–E).

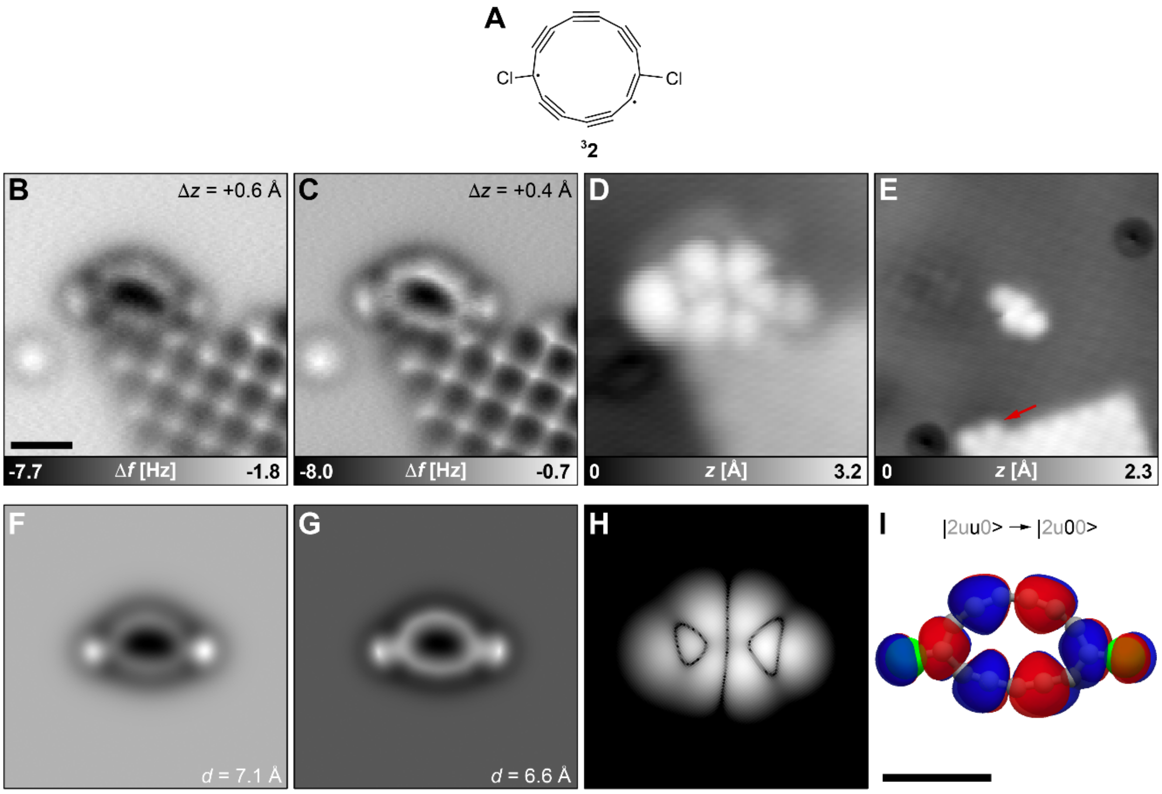

Figure S16. AFM, STM and orbital density image of ^{3}2. (**A**) Resonance structure of ^{3}**2**. (**B**, **C**) AFM data of ^{3}**2** at $\Delta z = 0.6$ Å (AFM-far) and $\Delta z = 0.4$ Å (AFM-close), respectively. Setpoint: $V = 0.2$ V, $I = 1.2$ pA. (**D**) STM orbital density image of ^{3}**2** at the PIR ($V = –0.54$ V, $I = 0.5$ pA). Image size (B–D) 28 x 28 Å^{2}, scale bar 5 Å in (B), applies also to (C, D, F, G, H). (**E**) STM data after the molecule had been manipulated away from the step edge and is in the ^{1}**2-P** state. $V = –0.1$ V, $I = 0.7$ pA, image size 60 x 60 Å^{2}. The red arrow indicates a Cl atom of the 3rd layer NaCl island. The observation that this Cl remained at its position at the island, after lateral manipulation of the molecule off the island edge indicates that this Cl is part of the 3rd layer NaCl island and was not covalently bound to the molecule in (B–D). This is not obvious from the AFM images alone, because relaxations of the CO tip can give rise to apparent bonds at small tip-sample distances (*39, 42*), see (C). (**F**, **G**) AFM simulations (*39*) of ^{3}**2** in its relaxed adsorption geometry on NaCl (see **fig. S15**), with the image plane parallel to the molecular plane to account for the adsorption parallel to the surface. The adsorption geometry parallel to the surface is likely related to the molecule being at a NaCl step edge in (B) and (C), in contrast to the tilted adsorption geometry on defect-free NaCl. Simulations of AFM images were performed based on CASPT2 calculated xyz geometries using the Probe-

Particle Model (*39*) with default CO-tip parameters (stiffness $k_x = k_y = 0.25$ N/m, $k_R = 30$ N/m) at an oscillation amplitude of 0.5 Å. The distance *d* denotes the distance between the CO-tip's oxygen atom and the topmost atom of the molecule. **(H)** Simulated STM orbital density image (*43*) based on (**I**) the Dyson orbital of the transition from the neutral ^{3}**2** to the cation. Orbital densities of PIR and NIR of ^{3}**2**, simulated for different tip-sample distances, are shown in **fig. S26**.

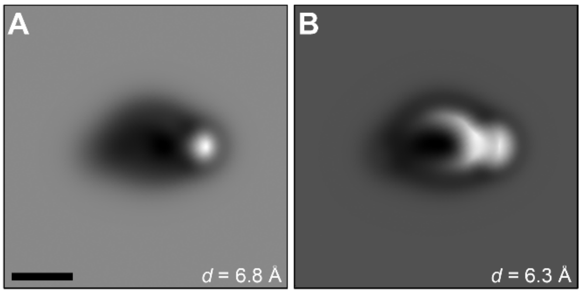

Figure S17. AFM simulations of ^{3}**2** in its relaxed adsorption geometry on NaCl using the Probe-Particle Model (*39*), with the image plane parallel to the surface. The tilted adsorption of ^{3}**2** on defect free NaCl (see **fig. S15**) is reflected in the image contrast, similar as in the AFM data shown in Fig. 6, A and D.

4.3. Transitions between configurations of **2**

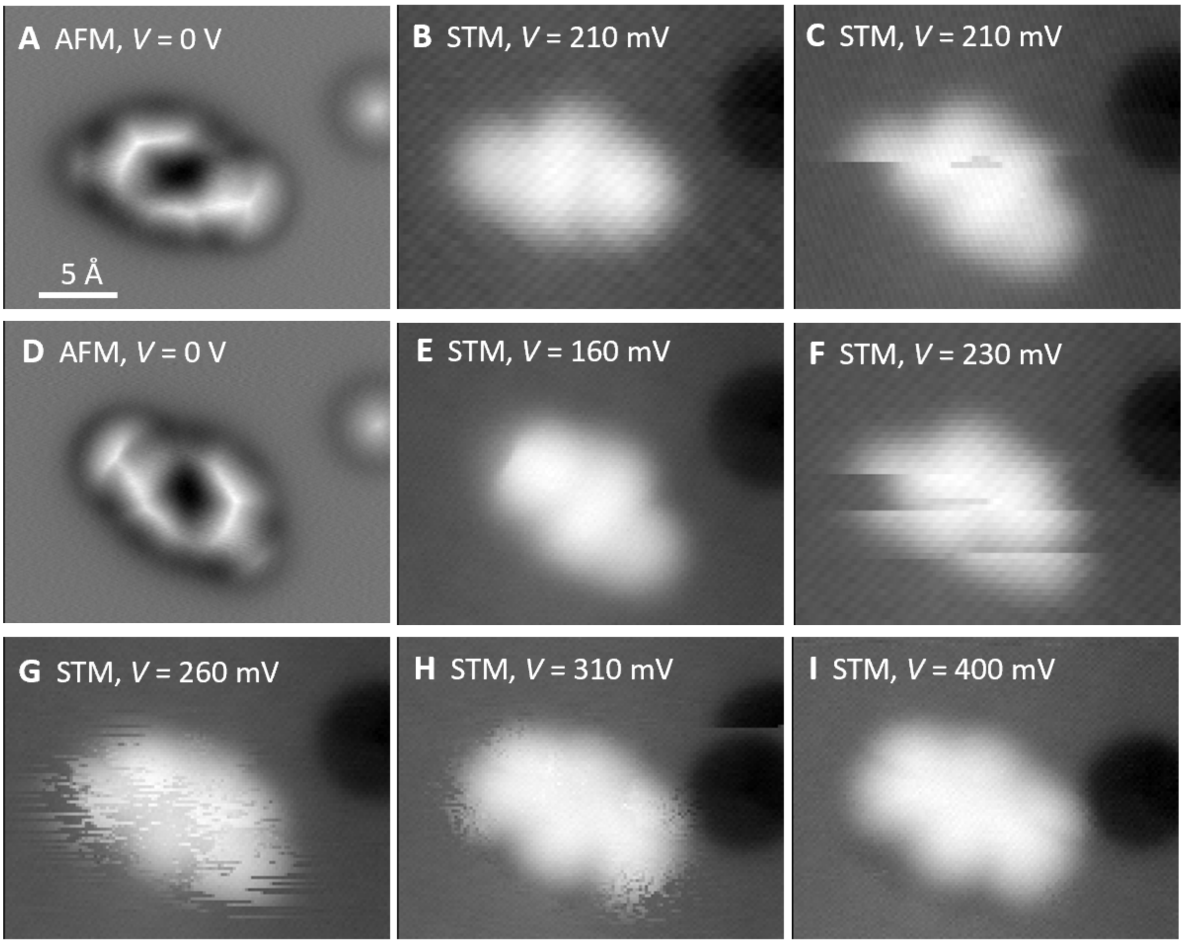

Figure S18. Sequence of AFM and STM data at different voltages. (**A**) Constant-height AFM data of ^{1}**2-M**. (**B**, **C**) STM images at $V = 210$ mV, that is, just at the threshold voltage for switching out of ^{1}**2-M** and ^{1}**2-P** states. Using these parameters, switching rates are on the order of minutes - about the timescale to acquire an STM image. We observed no switching of ^{1}**2-M** during the acquisition of (B) and one switching event from ^{1}**2-M** state to ^{1}**2-P** during the acquisition of (C). The slow scan direction is from top to bottom. (**D**) Constant-height AFM data of ^{1}**2-P**. (**E**) STM image of ^{1}**2-P** at $V = 160$ mV. For voltages below 200 mV we observed in general no switching events. (**F–I**) STM images at indicated voltages. By increasing V, the switching rate increased. At (F) $V = 230$ mV, few switching events between ^{1}**2-M** and ^{1}**2-P** can be observed in one image. In (G) and (H), obtained at $V = 260$ mV and $V = 310$ mV, respectively, many switching events result in noisy features within the images and the switching rate is faster than the typical time per scan line (on the order of seconds). In (I), at $V = 400$ mV, the switching rate is faster than the acquisition time per pixel (on the order of 10 ms), resulting in a smooth image. Note that the image shows two-fold symmetry. Next to **2** is a CO molecule, which moved by one lattice site during the acquisition of (H). All STM images were acquired at a constant current $I = 0.4$ pA. Scales from black to white, A [-3.4 Hz; +3.8 Hz], B [0 Å; +2.0 Å], C [0 Å; +2.0 Å], D [-3.3 Hz; =3.9 Hz], E [0 Å; +2.1 Å], F [0 Å; +2.1 Å], G [0 Å; +2.1 Å], H [0 Å; +2.1 Å], I [0 Å; +1.9 Å]. Scale bar in (A) applies to all images.

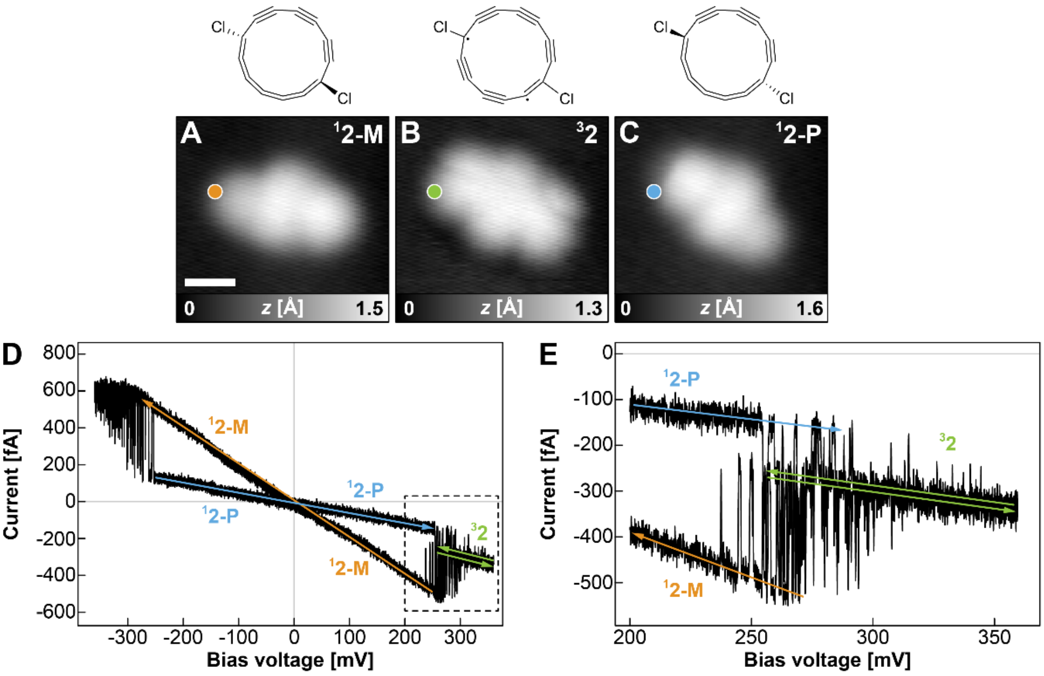

Figure S19. *I*(*V*) spectroscopy of transitions. (**A–C**) STM images and corresponding structures in the states of ^{1}**2-M**, (predominantly in) ^{3}**2**, and in ^{1}**2-P**, respectively. The position at which the *I*(*V*) spectra have been acquired is indicated. Scale bar in (A) is 5 Å and applies also to (B) and (C). Parameters for in (A) and (C) $I = 0.4$ pA, $V = 150$ mV that is, below the switching threshold. But for (B) $I = 0.4$ pA, $V = 400$ mV, that is, well above the switching threshold. As setpoint for the spectroscopy we chose $V = 400$ mV (STM parameters as in (B)), to be in the region of fast switching, with no measured telegraph noise, resulting in a well-defined tip height. (**D**) *I*(*V*) spectrum on **2** at the position indicated in (A, B, C). Setpoint $V = 400$ mV, $I = 0.2$ pA, $\Delta z = -0.25$ Å. The sample voltage *V* was ramped from 360 mV to -360 mV and back to 360 mV in 60 seconds. The occupation of either ^{1}**2-P** or ^{1}**2-M** in the region of small voltage (below the switching threshold) is stochastic. Here we show an example with different occupation during the down and up sweep of the voltage, to observe *I*(*V*) traces in both states. The intermittent current state, however, is never observed in the voltage region between the threshold voltages [-210 mV; +210 mV]. (**E**) Zoom into the indicated voltage range (dashed box in D). At large voltages ($V > 320$ mV) individual switching events cannot be observed, because the switching rate is too fast. The three current plateaus assigned to the three states are indicated. The measured currents at $V > 320$ mV correspond to the extrapolated currents of the intermediate current plateau in the voltage region where switching between all three current plateaus can be observed (250 mV to 270 mV), see green line. This observation is in line with the assumption that for $V > 320$ mV (large voltages, fast switching rates) the molecule is switching at a rate too fast to be detected by our STM, but most of the time resides in the ^{3}**2** state. This assumption is corroborated by the extracted lifetimes of ^{1}**2-P**, ^{1}**2-M** and ^{3}**2** as a function of current and voltage (**figs. S21** and **S22**). Switching between states ^{1}**2-P**, ^{1}**2-M** and ^{3}**2**, as observed for positive bias, was also observed at negative bias at similar absolute values of *V* (see D).

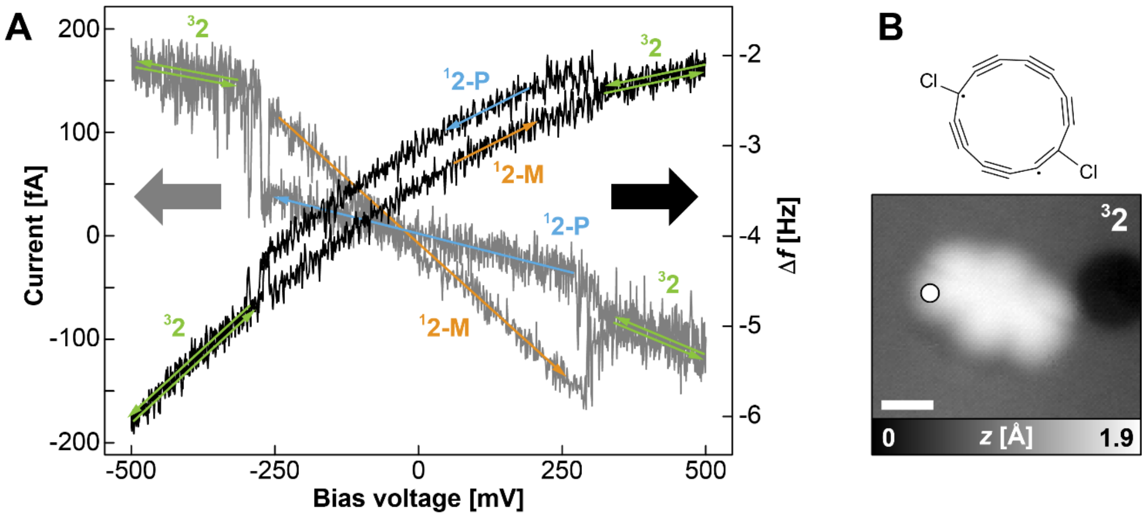

Figure S20: Kelvin probe force spectroscopy. (**A**) $I(V)$ spectrum (gray data, left y-axis) and simultaneously acquired $\Delta f(V)$ Kelvin probe force spectroscopy (KPFS, black data, right y-axis) on **2**. Setpoint $V = 400$ mV, $I = 0.3$ pA, $\Delta z = 0.5$ Å. V was ramped from 500 mV to -500 mV and back to 500 mV in 20 seconds. The configurations of **2** (for ^{3}**2**, the predominant configuration) for respective regions of the spectra are indicated. The KPFS spectra corresponding to all three configurations show parabolas that are only shifted in the vertical direction, implying that the charge state of **2** is the same in all three configurations (*78, 79*). Note that different charge-states were transiently accessed at increased voltages, when measuring at the onset of the ion resonances, that is the NIR of ^{1}**2** at $V = 1.0$ V (see Fig. 6F) and the PIR of ^{3}**2** at $V = -0.54$ V (see Fig. 6J and **fig.** S16). The vertical shift of the KPFS parabola corresponding to the ^{1}**2-P** configuration with respect to the other confirmations is explained by the different, non-voltage dependent background, mainly from van der Waals attraction and Pauli repulsion. The cantilever oscillation (amplitude $A = 0.5$ Å) was only switched on for this measurement to obtain KPFS data, but all other $I(V)$ spectra shown were measured without cantilever oscillation. (**B**) STM image indicating the tip position at which spectra in (A) were acquired. STM parameters, $I = 0.3$ pA, $V = 400$ mV.

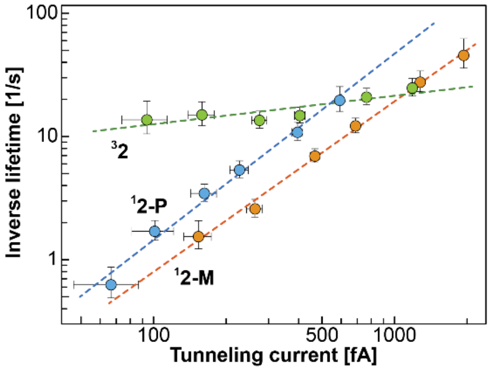

Figure S21. Switching rate as a function of tunneling current. Double logarithmic plot of the inverse lifetime, that is, the rate for switching out of the respective state, plotted against the current *I* measured in that state. The data is the same as shown in Fig. 5F. The raw data, *I*(*t*) traces, are shown in **fig. S23**. Data was obtained at *V* = 250 mV at constant tip heights with Δ*z* in the interval of Δ*z* = -0.25 Å (largest current of each state) to Δ*z* = +1.0 Å (smallest current of each state). Linear fits (dashed lines) yield slopes *k* of *k*(^{1}**2-M**) = 1.4, *k*(^{1}**2-P**) = 1.5, and *k*(^{3}**2**) = 0.2. These slopes indicate that transitions out of ^{1}**2-M** and ^{1}**2-P** are triggered by tunneling electrons in one- and/or two-electron processes (*80*), whereas the slope of transitions from ^{3}**2**, being much smaller than 1, indicates that transitions out of ^{3}**2**, are not primarily induced by tunneling electrons.

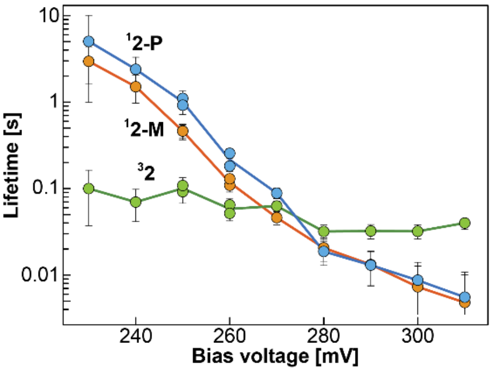

Figure S22. Lifetime as a function of *V*. Data was obtained at the same tip-height offset Δ*z* = 0.0 Å, but at different *V* in the interval *V* = 230 mV to *V* = 310 mV. The raw data, *I*(*t*) traces, are shown in **fig. S24**. For *V* = 250 mV and *V* = 260 mV, two measurements have been carried out, one before taking data at the other voltages and one after it, both are plotted to inquire reproducibility. We observe that for *V* > 280 mV, state ^{3}**2** has the longest lifetime and the molecule is most of the time in that state (see **fig. S24**). The small dependence of transitions out of ^{3}**2** as a function of *I* and *V* indicates that these transitions are not predominantly triggered by tunneling electrons and is tentatively explained with a spontaneous decay of the triplet with a lifetime on the order of 0.1 seconds or longer, which is moderately reduced by the applied electric field in the presence of the tip and/or tunneling electrons. The steep decrease of the switching rate with applied voltage for transitions out of ^{1}**2-M** and ^{1}**2-P** is in line with a transition triggered by tunneling electrons, that might evolve from a multiple-electron process at small voltages to a one-electron process with increasing yield at larger voltages (*80*).

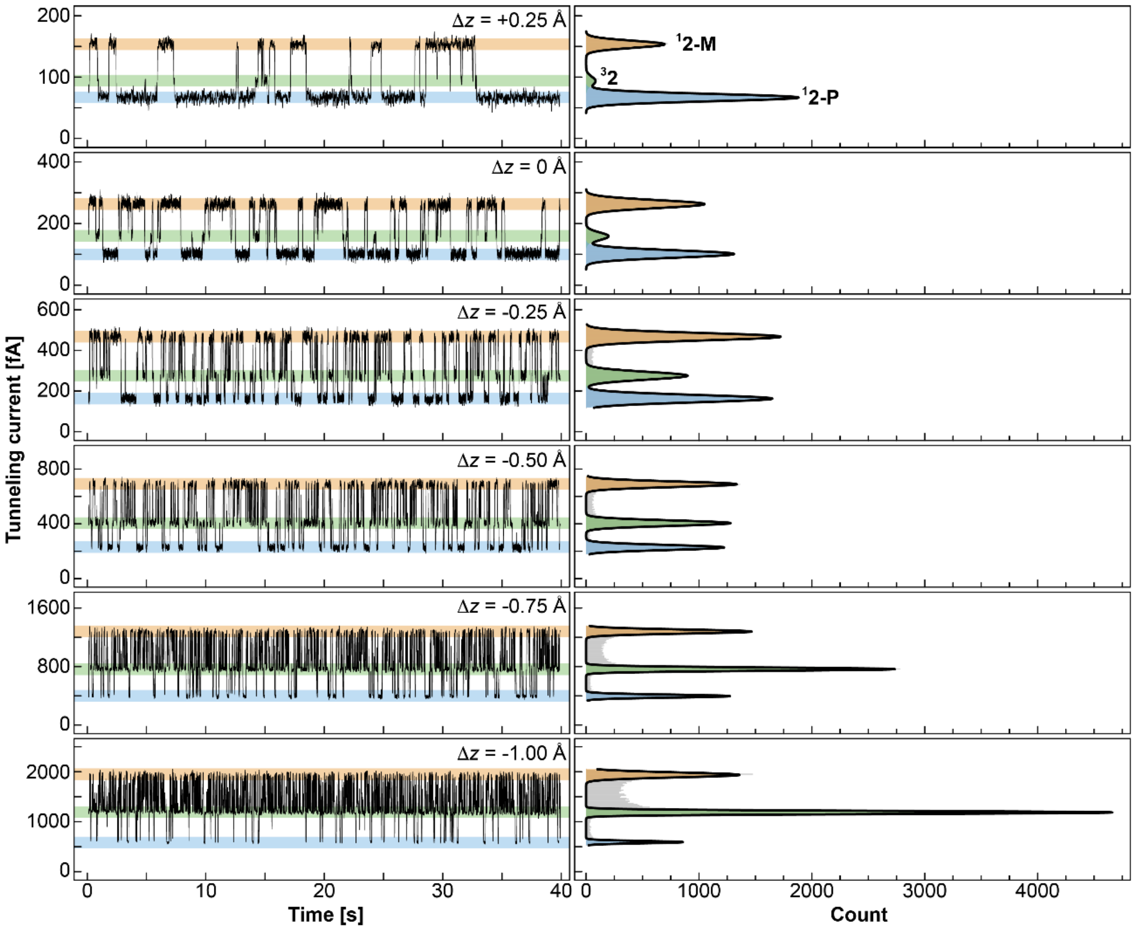

Figure S23. Raw *I*(*t*) data of transitions at different tip heights. Left-hand side panels: *I*(*t*) spectra at different tip-height offsets Δ*z* at constant *V* = 250 mV. The current plateaus assigned to the ^{1}**2-M state** (orange), the ^{3}**2** state (green) and the ^{1}**2-P** state (blue) are indicated by colors. Right-hand side panels show histograms of the currents (100 equally sized current bins for each spectrum). Counts refer to occurrences of currents for 1 ms (time bins), during a *I*(*t*) trace of 40 s.

The molecule cannot be imaged in the ^{3}**2** configuration at *V* = 0 V at this adsorption site, as it is not stable and decays with a lifetime on the order of 0.1 s. The assignment of ^{3}**2** is based on STM and AFM images at increased bias of ^{3}**2** at *V* > 300 mV, when the molecule is most of the time in that state, and its comparison with calculations (see **fig. S15**). These reveal that in the ^{3}**2** state the molecule is in either of two adsorption orientations. Moreover, the ^{3}**2** state is observed by STM and AFM on molecules at different adsorption sites at which the ^{3}**2** state was stable (see Fig. 6, A and D and **fig. S16**).

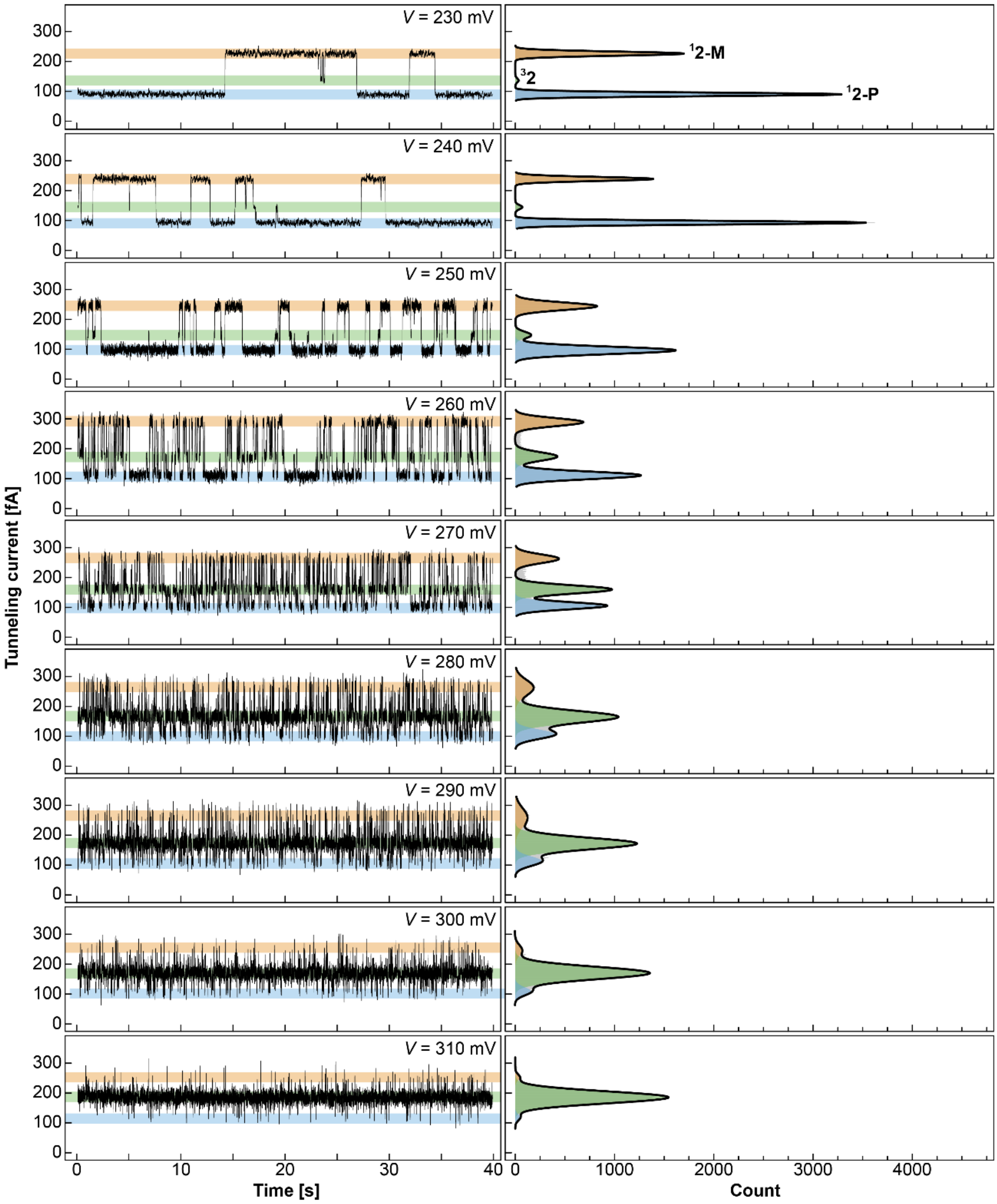

Figure S24. Raw *I*(*t*) data of transitions at different voltages. Left-hand side panels: *I*(*t*) spectra at different *V*, at constant tip-height offsets $\Delta z = 0$ Å. The current plateaus assigned to the ^{1}**2-M** state (orange), the ^{3}**2** state (green) and the ^{1}**2-P** state (blue) are indicated by colors. Right-hand side panels show histograms of the currents (100 equally sized current bins for each spectrum). Counts refer to occurrences of currents for 1 ms (time bins), during a *I*(*t*) trace of 40 s.

4.4. STM simulations

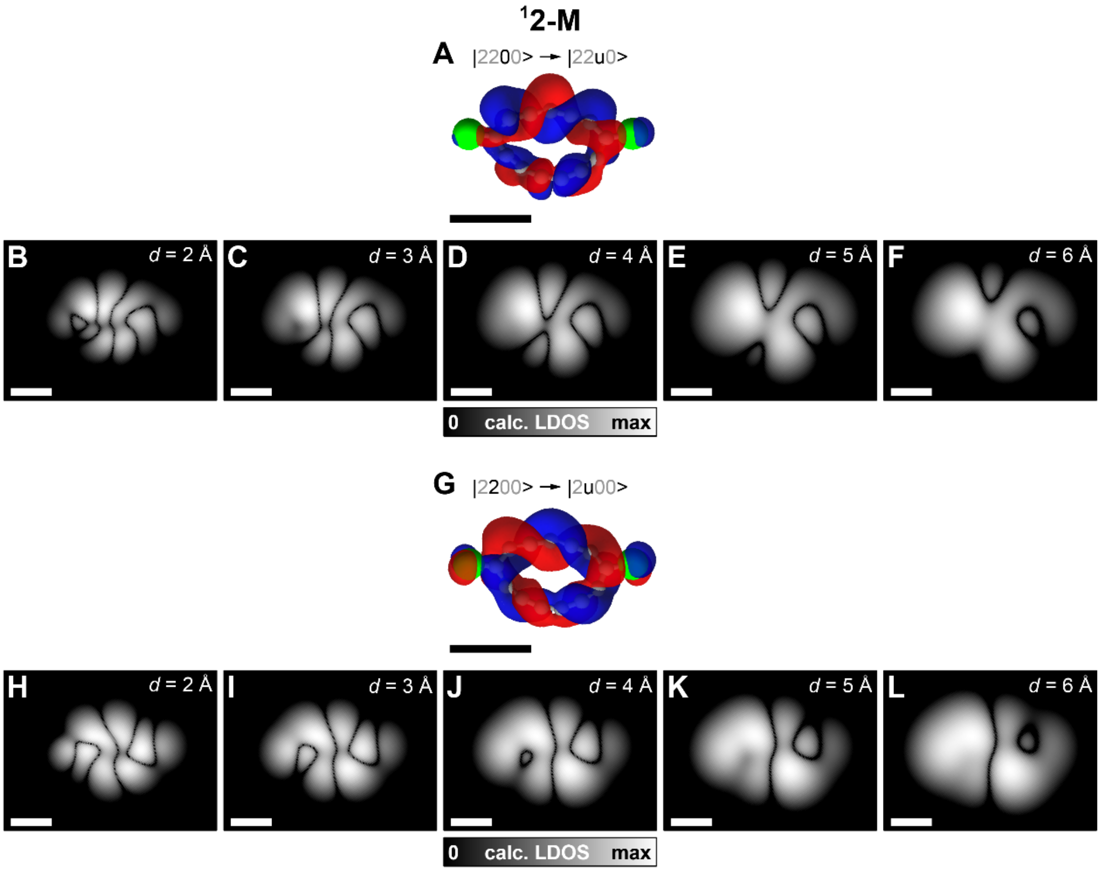

Figure S25. Simulated STM images of ionic resonances of ^{1}2-M. Simulations of STM images of ion resonances of ^{1}**2-M** based on Dyson orbitals for (**A**) the negative ion resonance (NIR) and (**G**) the positive ion resonance (PIR). The Dyson orbitals are used as inputs for simulating STM images. (**B-F**) Simulated STM images of the NIR based on the Dyson orbital for electron attachment to ^{1}**2-M** (A). (**H-L**) Simulated STM images of the PIR based on the Dyson orbital for electron detachment from ^{1}**2-M** (G). STM images have been simulated using Bardeen's tunneling theory, using an *s*-wave tip with a decay constant of 1 Å^{-1} and distances *d* between the upmost atom of $C_{13}Cl_2$ and the center of the wavefunction of the tip (*43*). Scale bars 5 Å.

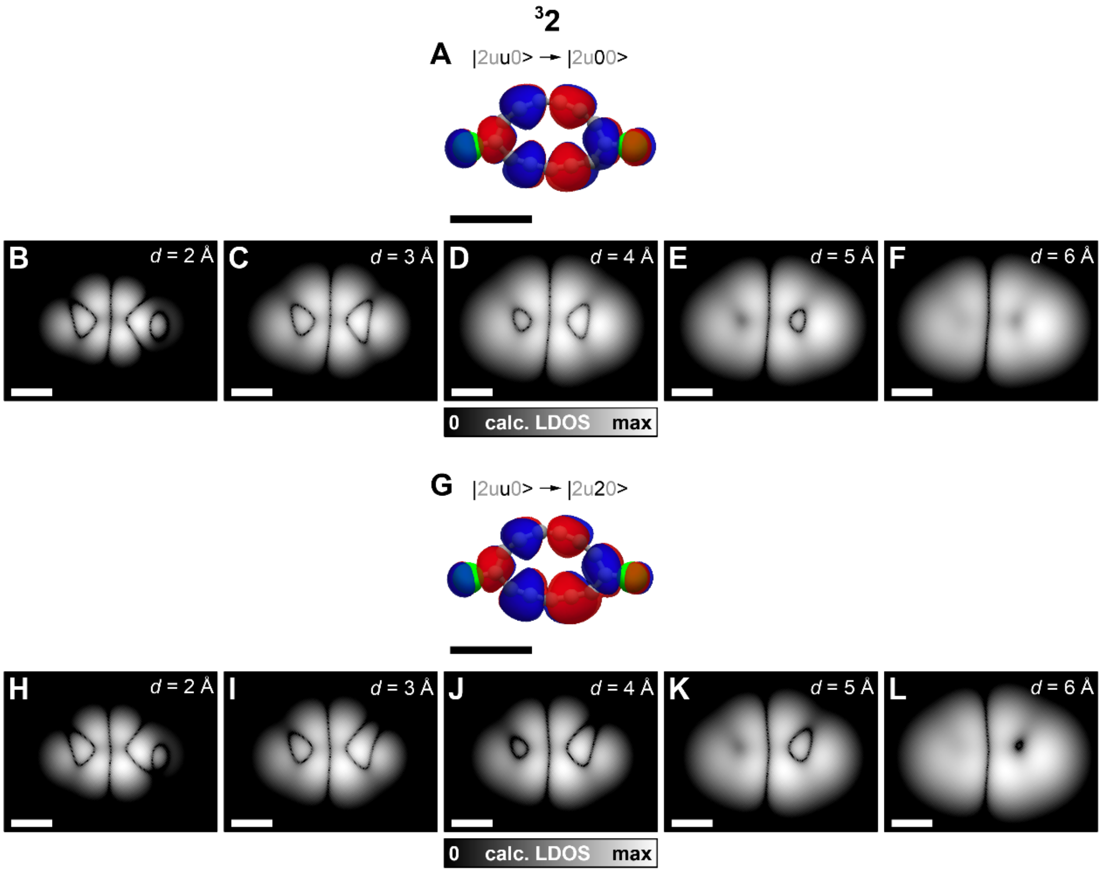

Figure S26. Simulated STM images of ionic resonances of ^{3}2. Simulations of STM images of ion resonances of ^{3}**2** based on Dyson orbitals for (**A**) the positive ion resonance (PIR) and (**G**) the negative ion resonance (NIR). The Dyson orbitals are used as inputs for simulating STM images. (**B**-**F**) Simulated STM images of the PIR based on the Dyson orbital for electron detachment from ^{3}**2** (A); (**H**-**L**) of the NIR based on the Dyson orbital for electron attachment to the out-of-plane system of ^{3}**2** (G) (*22*). STM images have been simulated using Bardeen's tunneling theory, using an *s*-wave tip with a decay constant of 1 Å^{-1} and distances *d* between the upmost atom of $C_{13}Cl_2$ and the center of the wavefunction of the tip (*43*). Scale bars 5 Å.

4.5. Graphical Summary

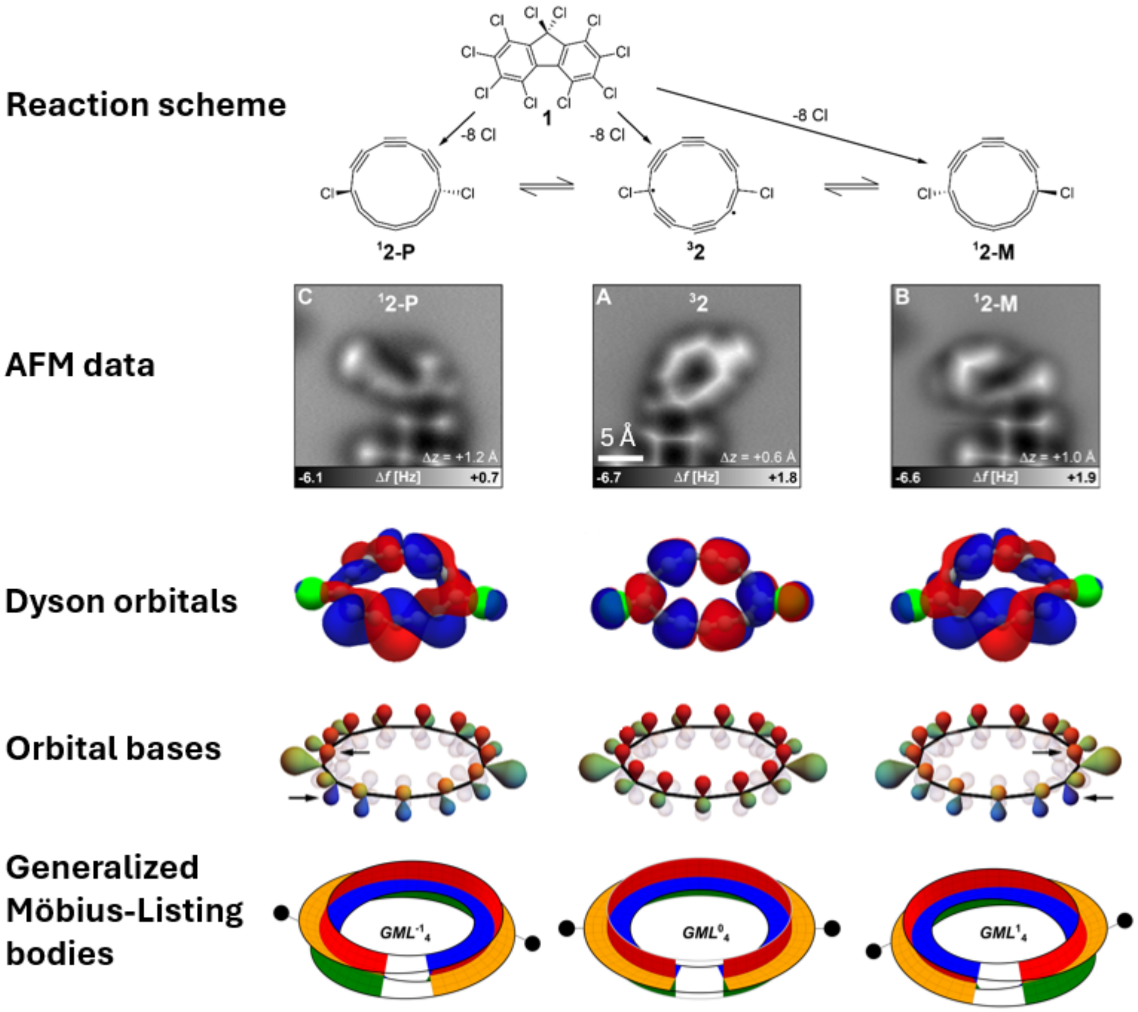

Figure S27. Graphical summary: Correspondence between molecular configuration, geometry, Dyson orbitals, orbital bases and generalized Möbius-Listing bodies. The first row shows the reaction scheme, see Fig. 2A. The second row shows AFM data, see Fig. 6, C, A and B. The third row shows Dyson orbitals obtained using CASPT2, see **figs. S9**. The shown Dyson orbitals, that is, electron attachment to the singlet and electron detachment from the triplet, correspond to the transitions accessed in STM measurements, see Fig. 6F and Fig. 6J. The fourth row shows the corresponding orbital bases, see Fig. 2, C, D and E. The fifth row shows the corresponding *GML* bodies, see Fig. 1, G, D, H in which schematic handles (black pins) have been added to highlight the correspondence to the Cl atoms and their out-of-plane distortions. The left column shows the singlet ^{1}**2-P**, the central column shows the triplet ^{3}**2** and the right column shows the singlet ^{1}**2-M**.

5. Supplementary Notes

5.1. Supplementary Note 1

The time-independent Schrödinger equation for a particle with mass *M* constrained on a ring with radius *r* can be written as:

$$\hat{H}\psi(\phi) = -\frac{\hbar^2}{2Mr^2}\frac{d^2\,\psi(\phi)}{d\phi^2} = E\psi(\phi) \tag{24}$$

where ϕ is the azimuthal angle. Solutions to Eq. 24 can be written as:

$$\psi_n(\phi) = \frac{1}{\sqrt{2\pi}}e^{\pm in\phi} \tag{25}$$

with *n* as a quantum number. The associated energies are:

$$E_n = \frac{n^2\hbar^2}{2Mr^2} \tag{26}$$

and the z-component of the angular momentum is:

$$\hat{L}_z\psi_n(\phi) = -\mathrm{i}\hbar\frac{d\,\psi(\theta\phi)}{d\phi} = \pm n\hbar \tag{27}$$

where the subscript *z* refers to the axis perpendicular to the ring, so that rotation about *z* changes ϕ.

If we assume that the wavefunction has the periodicity of 2π, i.e. it is single-valued for each angle ϕ:

$$\psi_n(\phi + 2\pi) = \psi_n(\phi) \tag{28}$$

$$e^{\pm in(\phi+2\pi)} = e^{\pm in\phi} \tag{29}$$

$$e^{\pm in2\pi} = 1 \tag{30}$$

This equality is satisfied for $n \in \mathbb{Z}$:

$$n_{\mathrm{H}} = 0, \pm1, \pm2, \pm3 \ldots \tag{31}$$

Where H in the subscript refers to the periodicity of 2π of a trivial (Hückel) system in Eq. 30. For a wavefunction with a periodicity of 8π, which corresponds to a quadruple-valued wavefunction in ϕ, analogously to Eq. 30 we obtain:

$$e^{\pm in8\pi} = 1 \tag{32}$$

which is satisfied for:

$$n_{8\pi\ \mathrm{periodic}} = \frac{n_{\mathrm{H}}}{4} = 0, \pm\frac{1}{4}, \pm\frac{2}{4}, \pm\frac{3}{4} \ldots \tag{33}$$

While this consideration is correct for a particle on a ring with a boundary condition of 8π, it may be an (overly) simplistic representation of a half-Möbius topology. A more sophisticated approach is shown in *Supplelmentary Note 2*, below.

5.2. Supplementary Note 2

In the cyclocarbons every carbon has two orthogonal *p*-orbitals contributing to the π system. This two-π-orbital-per-atom basis can be represented as a pseudospinor

$$|\psi\rangle = \begin{pmatrix} \psi_A \\ \psi_B \end{pmatrix}. \tag{34}$$

The boundary condition for making one circulation *C* in real space in the half-Möbius $GML^1{}_4$ topology is represented by

$$\boldsymbol{U_C} = \begin{pmatrix} 0 & 1 \\ -1 & 0 \end{pmatrix}. \tag{35}$$

Two full circumnavigations gives $\boldsymbol{U_C}^2 = -\boldsymbol{I}$, and hence a sign reversal of the spinor wavefunction, while the spinor wavefunction is periodic with respect to four full circumnavigations, $\boldsymbol{U_C}^4 = \boldsymbol{I}$. Using the Pauli matrix $\boldsymbol{\sigma_y}$, the boundary condition can be expressed as $\boldsymbol{U_C} = i\boldsymbol{\sigma_y}$, being a rotation on the Bloch sphere around the *y*-axis, accompanied by a global phase factor. Hence, the half-Möbius $GML^1{}_4$ topology entails a boundary condition with a wavefunction's sign change after *two* complete circumnavigations.

As shown in a prior work on Möbius graphene-based strips (*52*), boundary conditions resulting from a tight-binding Hamiltonian for a $GML^1{}_2$ body with *N* sites can be written as:

$$\hat{H} = -t\sum_{j=1}^{N} e^{i\frac{\gamma}{N}}(c_j^\dagger c_{j+1}) \tag{36}$$

In Eq. 34, the orbital basis acquires a shift of $\frac{\gamma}{N}$ between each site, resulting in an overall shift of γ over one circulation. In a Hückel topology ($GML^0{}_2$, Fig. 1, A and C), there is no phase shift and $\gamma = 0$, while in a Möbius topology ($GML^1{}_2$, Fig. 1, B and E) the wavefunction changes sign upon one circulation, meaning that $\gamma = \pi$.

The boundary conditions imposed in Eq. 36 are equivalent to an (effective) Aharonov-Bohm flux quantized in units of $\frac{\phi}{\phi_0}$ and resulting from a perpendicular magnetic field *B* applied to a particle on a ring with radius *R* (*53*),

$$\hat{H} = -t\sum_{j=1}^{N} e^{i\frac{2\pi\Phi}{N\Phi_0}}\left(c_j^\dagger c_{j+1}\right);\ \gamma = \frac{2\pi\phi}{\phi_0} \tag{37}$$

where $\Phi = B\pi R^2$ is the magnetic flux relative to the Dirac flux quantum $\Phi_0 = h/e$. As shown by Berry, γ is the geometric (Berry) phase accumulated upon one circumnavigation of the ring (*51*). Generalizing this analogy suggests that a $GML^n{}_m$ body may be characterized as having a Berry phase of $\gamma = \frac{2\pi\, n}{m}$. However, the Berry phase is only well defined, if interference effects become observable, that is, only after *two* full circumnavigations for a $GML^1{}_4$ body. The practical implications of such Aharonov-Bohm fluxes and Berry phases in real cyclocarbons with pseudospinor wavefunctions, where hopping terms between the ψ_A and ψ_B subsystems of nearest-neigbor atoms become nonzero, remain yet to be explored.